The Astrophysical Journal Letters, 1003:L15 (16pp), 2026 May 20 https://doi.org/10.3847/2041-8213/ae63bd

The Longest-period Young Transiting Exoplanets—A Duo of Puffy Giants inside a Debris Disk*

Carlos del Burgo[1,2], Alejandro Suárez Mascareño[1,2], Ana Heras[3], Jonathan P. Marshall[4], Peter J. Wheatley[5,6], Edward M. Bryant[5,6], Samuel Gill[5,6], Jorge Fernández Fernández[5,6], David R. Anderson[7], Matthew P. Battley[8,9], Edward Gillen[8], Solène Ulmer-Moll[9,10], James McCormac[5,6], Monika Lendl[9], Ioannis Apergis[5,6], Faith Hawthorn[5,11], James S. Jenkins[12,13], Maximiliano Moyano[7], Louise D. Nielsen[14], Alexis M. S. Smith[15], Suman Saha[12,13], Stéphane Udry[9], Jose I. Vines[7], Richard G. West[5,6], Daniel Bayliss[5,6], Hugh P. Osborn[16,17], Tristan Guillot[18], Amaury H. M. J. Triaud[19], Olga Suarez[18], Matteo Beltrame[20,21], Abdelkrim Agabi[18], Isabella Pagano[22], Matthew J. Hooton[23], Matthew R. Burleigh[24], Lyu Abe[18], Philippe Bendjoya[18], Georgina Dransfield[19,25,26], and Djamel Mékarnia[18]

[1] Instituto de Astrofísica de Canarias, Vía Láctea S/N, La Laguna, E-38200, Tenerife, Spain; cburgo@ll.edu.es, alejandro.suarez.mascareno@iac.es
[2] Departamento de Astrofísica, Universidad de la Laguna, La Laguna, E-38200, Tenerife, Spain
[3] European Space Agency (ESA), European Space Research and Technology Centre (ESTEC), Keplerlaan 1, 2201 AZ Noordwijk, The Netherlands; Ana.Heras@esa.int
[4] Academia Sinica Institute of Astronomy and Astrophysics, 11F of AS/NTU Astronomy-Mathematics Building, No.1, Sect. 4, Roosevelt Rd, Taipei 106319, Taiwan
[5] Department of Physics, University of Warwick, Gibbet Hill Road, Coventry, CV 4 7AL, UK
[6] Centre for Exoplanets and Habitability, University of Warwick, Gibbet Hill Road, Coventry, CV 4 7AL, UK
[7] Instituto de Astronomía, Universidad Católica del Norte, Angamos 0610, 1270709, Antofagasta, Chile
[8] Astronomy Unit, Queen Mary University of London, London, E1 4NS, UK
[9] Observatoire Astronomique de l'Université de Genève, Chemin Pegasi 51, CH-1290 Versoix, Switzerland
[10] Leiden Observatory, Leiden University, P.O. Box 9513, 2300 RA Leiden, The Netherlands
[11] Rugby School, Lawrence Sheriff St, Rugby, Warwickshire, CV 22 5EH, UK
[12] Instituto de Estudios Astrofísicos, Facultad de Ingeniería y Ciencias, Universidad Diego Portales, Av. Ejército Libertador 441, 8370191, Santiago, Chile
[13] Centro de Excelencia en Astrofísica y Tecnologías Afines (CATA), Camino El Observatorio 1515, 7591245, Las Condes, Santiago, Chile
[14] University Observatory, Faculty of Physics, Ludwig-Maximilians-Universität München, Scheinerstr. 1, 81679 Munich, Germany
[15] Institute of Space Research, German Aerospace Center (DLR), Rutherfordstr. 2, 12489, Berlin, Germany
[16] Center for Space and Habitability, University of Bern, Gesellschaftsstrasse 6, 3012 Bern, Switzerland
[17] ETH Zurich, Department of Physics, Wolfgang-Pauli-Strasse 2, CH8093 Zurich, Switzerland
[18] Observatoire de la Côte d'Azur, Université Côte d'Azur, CNRS, Laboratoire Lagrange, Bd de l'Observatoire, CS 34229, 06304, Nice cedex 4, France
[19] School of Physics & Astronomy, University of Birmingham, Edgbaston, Birmingham, B15 2TT, UK
[20] Istituto di Scienze Polari del CNR (ISP-CNR), Università Ca' Foscari, Via Torino n. 155, 30172 Venezia Mestre (VE), Italy
[21] Programma Nazionale di Ricerche in Antartide (PNRA), Institut polaire français Paul-Émile Victor (IPEV), France
[22] Istituto Nazionale di Astrofisica, 00136 Roma, Italy
[23] Cavendish Laboratory, JJ Thomson Avenue, Cambridge, CB3 0HE, UK
[24] School of Physics and Astronomy, University of Leicester, Leicester, LE1 7RH, UK
[25] Department of Astrophysics, University of Oxford, Denys Wilkinson Building, Keble Road, Oxford, OX1 3RH, UK
[26] Magdalen College, University of Oxford, Oxford, OX1 4AU, UK
Received 2025 December 31; revised 2026 March 24; accepted 2026 March 30; published 2026 May 18

Abstract

We identify two large-radius planets around the F-type star HD 114082 as the longest-period young transiting exoplanets known. From the first transit, detected by NASA's Transiting Exoplanet Survey Satellite (TESS), and a second dip, spotted by the Next-Generation Transit Survey (NGTS), we predicted midtransit times for HD 114082 b (planet b). We pinpoint its orbit (period $P_b = 225.5504 \pm 0.0004$ days) from a third transit captured with the ESA's CHaracterising ExOplanet Satellite and the upgraded Antarctic Search for Transiting ExoPlanets telescope (ASTEP+), alongside orbit-discriminating observations. Another dimming partly covered by ASTEP+ completes the four-transit series. We support with dynamical evidence the planetary nature of a deeper transit detected with TESS and NGTS, identifying planet c. Additionally, we reexamine the debris disk, fitting its excess emission with two dust components. Fundamental stellar parameters are inferred from stellar evolution models, while a joint modeling of photometric and radial velocity time series yields the planetary parameters, with masses further constrained using an N-body code. For planet b, the semimajor axis $a_b = 0.791 \pm 0.008$ au, eccentricity $e_b \approx 0$, inclination $i_b = 89.^{\circ}791 \pm 0.014$, radius $R_b = 1.046 \pm 0.014$ R_J, and 95% confidence upper limit on its mass $M_{95\%,b} = 1.6$ M_J. For planet c, $a_c = 0.99^{+0.03}_{-0.04}$ au, $e_c \approx 0$, $i_c = 89.^{\circ}701 \pm 0.011$, $R_c = 1.36 \pm 0.03$ R_J, and

* This study uses CHaracterising ExOplanet Satellite data observed as part of the Guest Observers programmes CH_PR240025 (PI: C. del Burgo) and CH_PR250012 (PI: C. del Burgo) and the Guaranteed Time Observation programmes CH_PR100017 and CH_PR140079.

$M_{95\%,c} = 2.0\ M_J$ (0.24 M_J if adding transit-timing-variation constraints). They seem to be moderate-to-low-mass giants in nearly resonant, coplanar, circular orbits that formed in situ, or beyond the snow line, and migrated inward, shaping the disk.

Unified Astronomy Thesaurus concepts: Exoplanets (498); F stars (519); Debris disks (363)

Materials only available in the online version of record: data behind figures

1. Introduction

The standard model for giant-planet formation (e.g., P. J. Armitage 2024; M. Ikoma & H. Kobayashi 2025) posits that giants form in gas-rich protoplanetary disks via a bottom-up process: submicron dust grains acquire ice mantles and coalesce into pebbles, planetesimals, and planetary cores that grow to their crossover mass, initiating runaway gas accretion. Core formation becomes challenging at semimajor axes $a \gtrsim 30$ au, where giants could form via gravitational instabilities in the disk. Accretion may occur in situ for planets as massive as a few Jupiter masses before being halted by a gas dispersal mechanism. The resulting system consists mainly of newly formed planets and a disk of dust and planetesimals (asteroids and comets), known as a debris disk, with a fractional dust luminosity $L_{\rm dust}/L_\star < 1\%$ and an age exceeding a few Ma (A. M. Hughes et al. 2018; Y. Hasegawa et al. 2022; C. Bergez-Casalou & Q. Kral 2024; S. Marino et al. 2026).

The bodies producing dust in debris disks are dynamically excited into a collisional cascade by a planetary companion(s), the most massive planetesimals in the disk, or some combination thereof (e.g., A. J. Mustill & M. C. Wyatt 2009; A. V. Krivov & M. Booth 2018; M. A. Muñoz-Gutiérrez et al. 2023; J. P. Marshall et al. 2026). However, the mechanisms and conditions driving planetary formation and evolution are not yet fully understood (e.g., J. Drążkowska et al. 2023; A. N. Youdin & Z. Zhu 2025).

Classical models suggest a crossover mass for runaway gas accretion of ∼20–30 $M_\oplus$, although ∼100 $M_\oplus$ has also been proposed (R. Helled 2023). Theory predicts that infant giant planets contract to their final size over hundreds of millions of years, while recent observations indicate planetary evolution may yield mature giants on timescales roughly 10 times shorter, though this remains debated (e.g., S. Benatti et al. 2021; A. Suárez Mascareño et al. 2021; O. Barragán et al. 2024).

Hydrodynamic simulations show that two giant planets, if they begin accreting simultaneously, end up with nearly identical masses after 0.5 Ma, irrespective of disk viscosity; whereas if one begins accreting later, their mass ratio initially peaks higher but quickly settles below 2 (C. Bergez-Casalou et al. 2023). This accounts for most observed systems with multiple gas-giant planets.

Through dynamical interactions, planets shape the radial and vertical structure of the underlying planetesimal belt (e.g., J. Terrill et al. 2023; T. D. Pearce et al. 2024; S. Marino et al. 2026), regardless of whether they undergo disk or tidal migration, dictating the formation and evolution of inner rocky planets (R. A. García et al. 2023; M. Best et al. 2024; Z. Kong et al. 2024; P. Sandhaus et al. 2025). Thus, planetary masses can be constrained from the spatially resolved architecture of a disk. Most evident in single-star systems, chaotic, resonant interactions between giant planets amplify destabilizations. Their scattering can disrupt planetary orbits, triggering migration, ejection, and engulfment by the star (D. Carrera et al. 2019).

Hot Jupiters represent ≈15% of known exoplanets, as their short orbital periods, large masses, and usually inflated radii enhance their detectability—despite a truly low occurrence rate of ≈2%; warm Jupiters appear to be as common as hot Jupiters, while the occurrence rate abruptly rises by about a factor of 4 for cold Jupiters, at $a \gtrsim 1$ au, reaching ratios per 100 stars of $14.1^{+2.0}_{-1.8}$ and $8.9^{+3.0}_{-2.4}$ for a in the ranges of 2–8 au and 8–32 au, respectively (B. J. Fulton et al. 2021). Thus, giant planets are rare, especially in pairs (R. A. Wittenmyer et al. 2020), and challenging to detect if orbiting young stars, because of strong stellar variability. For ages $\lesssim$100 Ma, most planets tend to be puffed-up, Neptune-mass planets, which formed in situ (A. Karalis et al. 2025).

The discovery and study of a statistically meaningful sample of planets as a function of age is still necessary to understanding their origin and evolution. In particular, transiting planets in multiple systems offer a wealth of information, as their masses and radii can be accurately determined, constraining their composition.

HD 114082, a young F-type star, originally was reported to host a Jupiter-sized planet (hereafter, planet b) with an orbital period $P = 109.8 \pm 0.4$ days ($a \approx 0.5$ au), eccentricity $e = 0.40 \pm 0.04$, and mass $M = 8.0 \pm 1.0\ M_J$ (O. V. Zakhozhay et al. 2022). These results pointed out that this could be the longest-period and most massive among the youngest known transiting exoplanets. N. Engler et al. (2023) revised planet b's orbital period as $P = 197^{+171}_{-109}$ days, based on the Transiting Exoplanet Survey Satellite (TESS) Sector 38 light curve (with a monotransit) and additional data. HD 114082 also hosts an unresolved dusty structure with an ill-constrained stellocentric radius (0.8–18 au; C. H. Chen et al. 2014; H. Jang-Condell et al. 2015; T. Mittal et al. 2015) and an external (≈38 au), nearly edge-on, CO-free exo-Kuiper Belt, with a small vertical scale height in scattered light (Z. Wahhaj et al. 2016; Q. Kral et al. 2020; N. Engler et al. 2023; L. Matrà et al. 2025). The planes of the debris disk and planet b's orbit form an angle >6°, suggesting the known planet is dynamically interacting with other bodies within the belt (N. Engler et al. 2023). Indeed, the NASA Exoplanet Archive[27] (J. L. Christiansen et al. 2025) lists a candidate planet, TOI-6697.02 (hereafter, planet c), identified from a monotransit in TESS Sector 64.

In this Letter, we present the first results of a multitelescope follow-up campaign, which started with the Next-Generation Transit Survey (NGTS), after the TESS detection of a monotransit in HD 114082's light curve, and continued with the CHaracterising ExOplanet Satellite (CHEOPS), the Las Cumbres Observatory (LCO) network, and the Antarctic Search for Transiting ExoPlanets telescope (ASTEP+), aimed at constraining the characteristics of the two planets in the system. Section 2 is devoted to the host star. Section 3 describes the observations and data preparation, including

[27] https://exoplanetarchive.ipac.caltech.edu

Table 1
For Each Facility Used, the Median Cadence, Number of Points (N), rms (Average over All Epochs), and Uncertainty (σ), for Original and 5 minutes Binned Light Curves, as Well as the rms after Model Subtraction (rms_{res})

Facility	Cadence (s)	N	rms (ppt)	σ (ppt)	Cadence (s)	N_{bin} (ppt)	rms_{bin} (ppt)	σ_{bin} (ppt)	rms_{res} (ppt)
CHEOPS	19.8	14,126	1.4	0.23	300	1212	1.5	0.06	0.21
TESS	120	70,941	0.7	0.6	300	28,494	0.7	0.4	0.25
NGTS	13	175,886	6	6	300	7920	2.0	1.2	1.1
ASTEP+ (R)	7.4	38,756	7	1.7	300	1189	1.7	0.28	1.1
LCO	4.9	7205	5	1.0	300	257	2.0	0.8	0.8

ancillary data. Section 4 shows our analysis and results, Section 5 discusses them, and Section 6 lists our conclusions. Appendices A, B, C, D, and E respectively include further details of the stellar and planetary characterization, transit-timing variations (TTVs), nature of planet c, and system architecture, while Appendix F provides additional tables.

2. The Host Star

HD 114082 is a bright ($G = 8.1060 \pm 0.0028$), young (15 ± 3 Ma), fast-rotating ($v \sin i = 39.2 \pm 0.5$ km s^{-1}) F3 star with an effective temperature of 6600 ± 70 K, at a distance of 95.06 ± 0.20 pc, being part of the Lower Centaurus Crux subgroup in the Scorpius–Centaurus OB Association, which hosts low-density, unbound, star-forming regions (Gaia Collaboration et al. 2016, 2023; J. Gagné et al. 2018; E. A. Avallone et al. 2022; O. V. Zakhozhay et al. 2022; V. Squicciarini et al. 2025). The key parameters of HD 114082 are presented in Appendix A, including those derived to characterize its planets.

3. Observations and Data Preparation

Observations from several facilities and ancillary public data are used to yield precise photometric time series of HD 114082 (Sections 3.1–3.5). Every light curve provides a reliable measurement of a broadband flux change over time, enabling the detection of small variations. For ground-based observations, we applied differential photometry relative to nearby nonvariable comparison stars, which minimizes atmospheric and instrumental effects on the observed flux, isolating astrophysical signals and improving photometric precision. In contrast, space observations are free from scintillation noise and are unaffected by the day–night cycle or cloud cover. Table 1 includes the photometric precision achieved with each facility before and after light-curve binning. We also use public time-series spectra of our target (see Section 3.6).

3.1. TESS

NASA's TESS satellite (G. R. Ricker et al. 2014) employs four widefield cameras with a 10 cm effective aperture size to perform a survey of 85% of the sky degrees in 30 partially overlapping sectors of $24° \times 96°$ (combined field of view or FOV), each observed for two orbits in the 600–1000 nm bandpass. The pixel size is $21''$ and the FWHM of the point-spread function (PSF) is nearly $30''$.

We use public data of Sectors 38 (from 2021 April 28 to 2021 May 26), 64 and 65 (from 2023 April 6 to 2023 June 2), and 99 (from 2026 January 5 to 2026 February 2), corresponding to HD 114082 (TESS magnitude of 7.8), with a 2 minutes cadence, and discard data from Sector 11, because the star's signal is obscured. Light curves are generated by the TESS Science Processing Operations Center (SPOC). The SPOC pipeline (J. M. Jenkins et al. 2016) first calibrates science data by orbit and then by sector, extracting high-precision time-series photometry for selected targets (D. A. Caldwell et al. 2020). TESS light-curve files provide time stamps and fluxes from the simple aperture photometry (SAP) and the presearch data conditioning corrected SAP (PDCSAP; J. C. Smith et al. 2012; M. C. Stumpe et al. 2012, 2014). The SAP flux is calculated by summing all calibrated pixels in the optimal (highest signal-to-noise ratio or S/N) aperture, whereas the PDCSAP flux is corrected for instrumental long-term trends. Our analysis is based on the PDCSAP flux. Aperture photometry on the crowded field around our target yields a transit depth dilution that was corrected to avoid underestimating the planetary radii (see Section 4.2 and Appendix B).

3.2. CHEOPS

ESA's first small-class mission, CHEOPS (N. Rando et al. 2020; W. Benz et al. 2021), is conducting high-precision photometry in the 330–1100 nm bandpass using a 30 cm telescope, from a Sun-synchronous, dusk–dawn orbit at 700 km above Earth. The FOV of $19' \times 19'$ rotates around the line of sight once per orbit ($P = 98.7$ minutes), the pixel size is $1''$, and 90% of the total energy of the defocused PSF is within a radius of 16 pixels. This avoids the saturation of bright stars onto the detector and enables the performing of high-precision photometry of one target at a time without significant contamination.

We present Fourth Announcement of Opportunity (AO-4) cycle observations of Guest Observers (GO) program PR240025 (PI: C. del Burgo) and AO-5 cycle GO program PR250012 (PI: C. del Burgo), aimed at determining the key parameters of planet b. Critical time observations at 30 s cadence were made on 2024 June 5, targeting an orbital period alias identified from an NGTS transit detection on 2023 March 11 (see Section 3.3). In addition, we present public data from Guaranteed Time Observers (GTO) programmes PR100017 and PR140079, to complement the target's observations. Data were processed at the Science Operations Centre from the CHEOPS Data Reduction Pipeline (S. Hoyer et al. 2020). Appendix F lists the CHEOPS programmes. To produce a roll-angle detrended light curve, we followed the procedure outlined by P. F. L. Maxted et al. (2022).

3.3. NGTS

NGTS (P. J. Wheatley et al. 2018), located at the ESO Paranal Observatory in Chile, uses an array of 12 robotic 20 cm telescopes to perform high-precision photometry of exoplanet transits in the 520–890 nm bandpass.

In order to follow up the TESS detection of a single transit of planet b, one NGTS telescope monitored HD 114082 during 167 nights between 2023 February 17 and 2023 September 6. The second transit of planet b was captured on 2023 March 11, and the first transit of planet c was detected, concurrently with TESS, on 2023 April 29. NGTS observations resumed on 2023 December 6, with another 47 nights of observations accumulated by 2024 August 19.

Due to the star's brightness, the telescope was defocused to produce a donut-shaped PSF with a radius of approximately 6 pixels (30″), preventing detector saturation. Observations with 10 s exposure time and ∼13 s cadence were made continuously for as long as the target was visible above an elevation of 30°. Precise autoguiding was carried out using the science images and the DONUTS algorithm (J. McCormac et al. 2013).

Differential photometry was performed using a 6 pixel radius aperture for HD 114082 as well as 100 comparison stars from across the 8 deg^2 field that were selected to match the target brightness and color as closely as possible. The resulting light curves were filtered for cloudy intervals and detrended against airmass to account for color differences between the target and the averaged comparison stars.

3.4. ASTEP+

ASTEP+ (N. Crouzet et al. 2020; G. Dransfield et al. 2022; F.-X. Schmider et al. 2022) is a 40 cm aperture telescope located near Concordia Station, at Dome C (on the Antarctic Plateau, at an elevation of 3234 m). In 2021, the telescope received a major upgrade of its camera system (F.-X. Schmider et al. 2022). It now operates with two high-sensitive cameras, providing simultaneous photometry in a blue channel (central wavelength λ_c of 555 nm and bandwidth $\Delta\lambda$ of 293 nm) and in a red channel (λ_c: 850 nm; $\Delta\lambda$: 276 nm). Real-time guiding is ensured in the blue channel. The FOV is nearly 40′ wide and the image scale is 1.″39 $pixel^{-1}$. Concordia Station experiences a near-continuous night (polar night) from mid May to late July, which benefits the target's monitoring. Time-critical observations were acquired on 2024 June 6 and 2024 September 25–26 and on 2025 May 8–10 and 2025 August 30, with exposure times of 60 s and 1 s for the blue and red channels, respectively. They were conducted under a polar night sky with a new moon in June (total darkness) or under nonpolar night conditions with significant lunar illumination on the three other dates (two shortly after the austral winter). Wind speeds ranged from 2 to 9 m s^{-1}. Here, we adopt the red (R) channel data, taken at a 7.4 s cadence.

Automated on-site data processing, including detrending, was conducted and promptly verified by inspecting the target's light curve and the target flux and systematics. These enable a near-instantaneous identification of transit events. The largest data product files—containing aperture photometry for up to 1000 stars in the field, observation metadata, and the stacked image generated during reduction—were later transferred to a local server. Data acquired in 2024 were finally transmitted to Europe, being reanalyzed.

3.5. The LCO Network

We use data from the LCO global telescope network (T. M. Brown et al. 2013). A Director's Discretionary Time program (DDT2025A-006; PI: C. del Burgo) was granted 30 hr to monitor HD 114082 on 2025 May 8–10, aimed at testing a candidate orbital period for planet b. The observations were performed at Cerro Tololo Inter-American Observatory with the 0.4 m telescope, equipped with QHY600 CMOS cameras. A 2 s exposure time in the V band and the default readout mode in a 30′ × 30′ FOV yielded sufficient comparison stars to calibrate the 7 s cadence light curve of HD 114082. Bad weather hindered observations most of the time. LCO archival data obtained in 2022 and 2023 complement the dataset. Appendix F provides detailed information about the different observing campaigns. All retrieved data products were processed using the BANZAI pipeline (C. McCully et al. 2018). We derive the light curves using the ELOY package,[28] which implements the algorithm from C. Broeg et al. (2005).

All available LCO time-series segments cover total durations shorter than the transits of planets b and c and do not show flux decreases that would indicate a transit ingress or egress. We select those sets of consecutive observations, and common filters for a given telescope, on which differential photometry could be performed, so that the resulting normalized fluxes represent relative variations within each set. Table 5 in Appendix F provides details of these observations. With gaps between consecutive observations exceeding the characteristic transit durations of planets b and c, the uniform relative flux levels confirm that all LCO data were acquired out of transit. These measurements provide additional constraints on the orbital periods of planets b (via the period alias testing) and c. In particular, the LCO light curves, together with those from NGTS, TESS, and CHEOPS, narrow the probability density function (PDF) of midtransit times for planet c and, thus, remarkably constrain its predicted orbital period (see Appendix B).

3.6. Fibre-fed Extended Range Optical Spectrograph and High Accuracy Radial velocity planet Searcher Spectra

We use the 4 yr monitoring campaign time-series spectra of HD 114082 obtained with the Fibre-fed Extended Range Optical Spectrograph (FEROS; A. Kaufer et al. 1999), conducted by O. V. Zakhozhay et al. (2022). We also employ the public spectra of the High Accuracy Radial velocity planet Searcher (HARPS; M. Mayor et al. 2003), previously used by O. V. Zakhozhay et al. (2022). We downloaded 54 FEROS spectra from the ESO archive,[29] while 18 HARPS spectra were retrieved from the Data & Analysis Center for Exoplanets.[30]

Both FEROS and HARPS are equipped with pipelines that yield extracted and wavelength-calibrated spectra. These reduced data were used to derive the radial velocity (RV) and bisector span curves with a Gaussian fit to the cross-correlation function (CCF) of each spectrum with the HARPS G2 mask (P. Fellgett 1955; A. Baranne et al. 1996; F. Pepe et al. 2000). Given the fast stellar rotation (causing significant line broadening), an RV range of ±200 km s^{-1} around the systemic velocity is used. Then, we sigma-clipped outliers with RVs larger than 500 m s^{-1}, yielding 48 FEROS RV data points (6 rejected) and 18 HARPS RV data points (none rejected). A quick look at the FEROS data revealed a weak correlation of the resulting velocities with ambient pressure. We detrended the RV measurements using a third-order polynomial against pressure. The resulting RVs show an rms

[28] https://github.com/lgrcia/eloy
[29] https://archive.eso.org
[30] https://dace.unige.ch

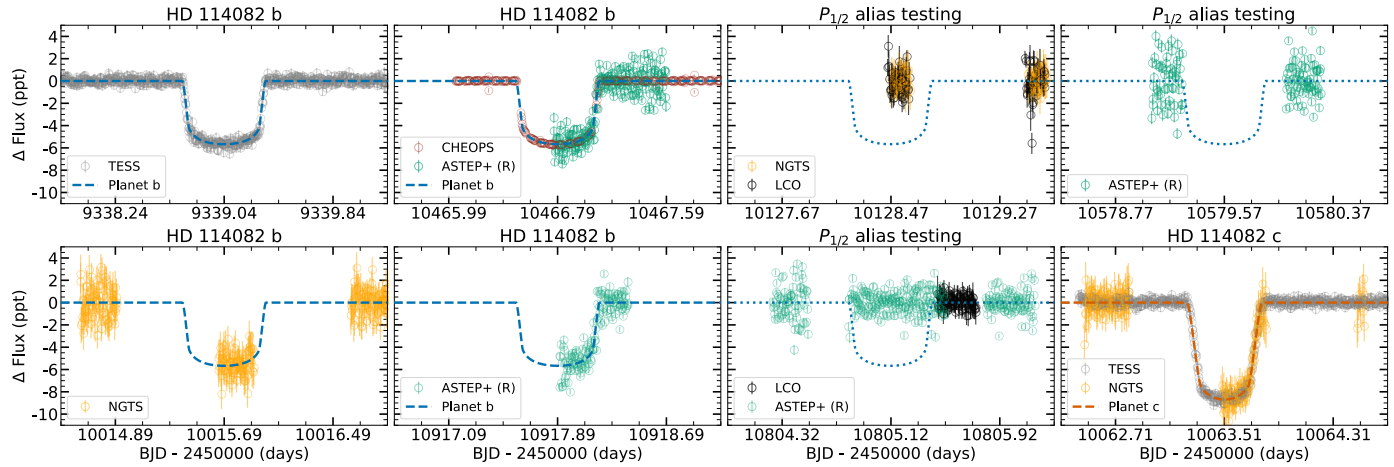

Figure 1. Binned light curves of HD 114082 during eight decisive events; the symbols and colors denote the facilities used. Left: four nonconsecutive transits of planet b, fully detected by TESS (first) and CHEOPS (third), and partly (≈50%) observed by NGTS (second) and ASTEP+ (third and fourth), with fitted model (blue dashed line). Center right and top right: period alias testing conducted using observations from ASTEP+, LCO, and NGTS, which ruled out the orbital period $P_{1/2}$ (≈112.78 days), with the expected dips (blue dotted lines) as a reference. Bottom right: transit of planet c observed by TESS (fully) and NGTS (over half), with fitted model (red dashed line). The data used to generate this figure are available in machine-readable format.

(The data used to create this figure are available in the online article.)

of 118 m s^{-1}, with a median uncertainty of 160 m s^{-1}, for FEROS, and 52 m s^{-1}, with a median uncertainty of 20 m s^{-1}, for the HARPS data. The fitting residuals are 18 m s^{-1} (HARPS) and 114 m s^{-1} (FEROS).

4. Analysis and Results

4.1. Planets b and c: Transit Observations

TESS detected two transits different in depth (δ) and duration (T_{14}) in HD 114082. The first of these, owing to planet b, was registered on 2021 May 4 in Sector 38. We inferred a series of candidate orbital periods for planet b from the lapse between this midtransit time (BJD $2459339.0380^{+0.0012}_{-0.0011}$) and that estimated from another dip of the same depth—detected by NGTS on 2023 March 11. We then predicted and observed a third transit—fully with CHEOPS and over half coverage with ASTEP+—on 2024 June 5, consistent with orbital period $P = 225.5504 \pm 0.0004$ days and its alias $P_{1/2}$= 112.77520 ± 0.00022 days. While the observing conditions on 2024 September 26 prevented a confident conclusion with ASTEP+, no dip was detected either on 2023 July 2 by NGTS and LCO or on 2025 May 8–10 by ASTEP+ and LCO, ruling out $P_{1/2}$, irrespective of any potential TTVs (see Appendix C). Subsequently, we observed another half a transit of planet b with ASTEP+, completing a series of four transits. See Figure 1.

The second TESS monotransit, due to planet c, occurred on 2023 April 29 (midtransit at BJD 2460063.5113 ± 0.0012) in Sector 64. The same transit was observed (over half) by NGTS, enhancing its planetary nature (see Appendix D), further supported by dynamical constraints as well as the observed alignment between the two planetary orbits and their misalignment with the outer belt's plane, reflecting planet–planet interactions.

4.2. Planetary System Parameters

We construct a global model of photometry and RV—incorporating a floating zero-point offset for each instrument, a linear trend for the RV curve, and linear trends for the RV against bisector span—and apply it to all available photometric and spectroscopic data. Short-term variability (both stellar and systematic) is described using Gaussian Process (GP) regression (C. E. Rasmussen & C. K. I. Williams 2006) with the S+LEAF code (J. B. Delisle et al. 2022), while planetary transit signatures and RV signals are represented using Pytransit (H. Parviainen 2015; see also K. Mandel & E. Agol 2002 for a description of the quadratic limb-darkening law) and sinusoidal functions, respectively. Given the large TESS pixel scale, we include a flux dilution factor. To avoid biasing the results toward any specific orbital period, we conduct a blind period search. The parameters are optimized using Bayesian inference with the nested sampling (J. Skilling 2004, 2006) code Dynesty (J. S. Speagle 2020; S. Koposov et al. 2023).

The model converges on a solution with two significant planetary signals that is consistent with zero eccentricity (e =0) for both planets. Table 2 lists the key planetary parameters for this solution, including the midpoint time of transit (T_0), orbital period (P), impact parameter (b), inclination (i), radius (R), and 95% confidence upper limit on the mass $M_{95\%}$, linked to the RV semiamplitude (K). The transits of planet b, combined with our period alias testing, firmly establish its period P_b. For planet c, the shape and duration of its transit, the stellar parameters, and the constraints from nontransit data reduce the 1σ uncertainty of P_c (ΔP_c) to <6% for the preferred circular model, although this uncertainty is higher for the eccentric model (Table 6 in Appendix F). For $e = 0$, $P_c/P_b = 1.39^{+0.05}_{-0.08}$, which encloses within 1σ the second-order 7:5 mean-motion resonance (MMR) and within 3σ the first-order 3:2 MMR. The latter is dynamically stronger and more stable, but the uncertainty in P_c prevents the establishing of an unequivocal link to any of these two MMRs, with $\Delta P_c \approx$ (0.5–0.8) ($P_{\frac{3}{2}}$–$P_{\frac{7}{5}}$). The planets could be nearly locked or locked, which shall be clarified eventually with further observations.

For a more detailed description of the applied method, see Appendix B. Table 6 in Appendix F lists the full set of parameters and priors of the models, including that for nonzero eccentricity.

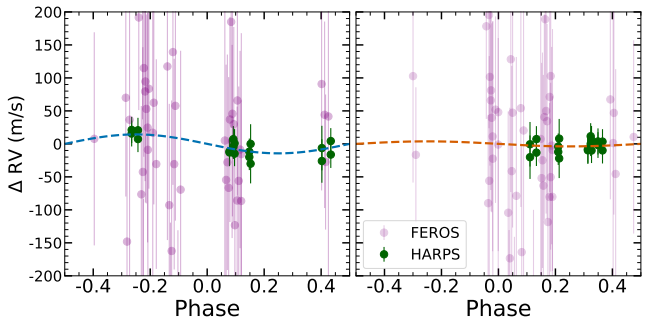

Figure 2. Phased detrended RVs of planet b (left) and planet c (right), inferred from our GP modeling—applied to the full dataset. The RV points in green and purple represent HARPS and FEROS, respectively. The data used to generate this figure are available in machine-readable format.
(The data used to create this figure are available in the online article.)

Table 2
Orbital and Physical Parameters of Planets b and c for the Preferred Solution (Circular Model)

Parameter	Planet b	Planet c
δ (%)	0.569 ± 0.003	0.87 ± 0.03
T_{14} (hr)	14.69 ± 0.05	13.18 ± 0.09
T_0 (BJD)	2460466.7909 ± 0.0017	2460063.5114 ± 0.0009
P (days)	225.5504 ± 0.0004	314^{+11}_{-18}
e	0 (fixed)	0 (fixed)
b	$0.421^{+0.022}_{-0.024}$	0.75 ± 0.10
i (deg)	89.791 ± 0.014	89.701 ± 0.011
$R/R_\star$	0.0714 ± 0.0005	0.0928 ± 0.0014
$a/R_\star$	115.6 ± 1.3	144^{+5}_{-6}
a (au)	0.791 ± 0.008	$0.99^{+0.03}_{-0.04}$
R (R_J)	1.046 ± 0.014	1.36 ± 0.03
$M_{95\%}$ (M_J)	<1.6	<2.0
$K_{95\%}$ (m s^{-1})	<44	<49
$\rho_{95\%}$ (g cm^{-3})	<1.7	<1.0
$log\ g_{p,95\%}$ (cgs)	<3.1	<2.3
$\rho_\star$ (g cm^{-3})	0.57 ± 0.02	

Note. $R_\star$ and $M_\star$ from Appendix A were used to derive R and a, and $M_{95\%}$ and $K_{95\%}$, respectively.

Figure 2 shows phased RV data with planetary models derived from the median masses of the posterior distribution.

4.3. System Architecture

We seek to constrain the location of the unresolved warm debris disk of HD 114082 (C. H. Chen et al. 2014; H. Jang-Condell et al. 2015; T. Mittal et al. 2015), using the spectral energy distribution (SED) in conjunction with the spatially constrained extent of the outer belt (N. Engler et al. 2023; L. Matrà et al. 2025). We adopt the stellar parameters from Appendix A to select the PHOENIX stellar photosphere model (P. H. Hauschildt et al. 1999) and scale it to the photometry in the optical and near-infrared from Tycho BV, Gaia, the Two Micron All Sky Survey, and the Wide-field Infrared Survey Explorer (E. Høg et al. 2000; M. F. Skrutskie et al. 2006; E. L. Wright et al. 2010; Gaia Collaboration et al. 2016, 2023), after proving the excellent match. Figure 3 shows all the photometry used in our analysis; ultraviolet photometry (E. Paunzen 2015) is included for completeness.

The excess emission is modeled as two dust components fitted to the mid-infrared to millimeter photometry taken from

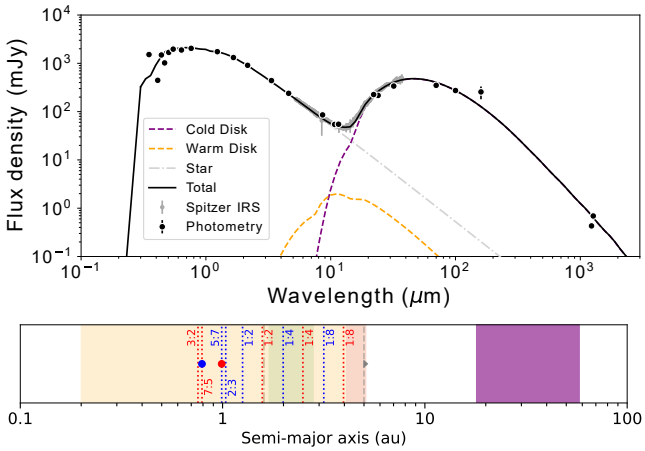

Figure 3. Top: SED of HD 114082, showing stellar photosphere (dotted–dashed gray curve), warm dust (dashed orange curve), cold dust (dashed purple curve), and total emission (solid black line) models, derived from literature photometry (black points) and the Spitzer/IRS spectrum (gray line). Bottom: schematic view of the HD 114082 system architecture, showing planet b (blue point) and planet c (red point), the respective MMRs and secular resonances (for $e = 0$; the red and blue dotted lines), the lower limit of the H_2O snow line (dashed gray line; estimated), the habitable zone for a 5 $M_\oplus$ planet from R. K. Kopparapu et al. (2014; shaded green region), and the locations of the inner warm belt (shaded orange region; estimated) and the spatially constrained exo-Kuiper Belt (shaded purple region: L. Matrà et al. 2025). Also, the maximum stellocentric radius for a potential transit (dotted–dashed line) is displayed.

AKARI (D. Ishihara et al. 2010), the Spitzer Infrared Spectrograph (IRS) and MIPS (C. H. Chen et al. 2014), Herschel PACS (G. Marton et al. 2024), and the Atacama Large Millimeter/submillimeter Array (ALMA; J. Lieman-Sifry et al. 2016; L. Matrà et al. 2025). We employ the CASSIS low-resolution spectrum from the IRS on board the Spitzer Space Telescope (V. Lebouteiller et al. 2011). See Appendix E for more details.

Because of growth and destruction processes, dust grains cover a broad size range, exhibiting different wavelength-dependent absorption, emission, and scattering behaviors. We adopt a power-law distribution for the number density $n(s) \propto s^{-q}$ (J. S. Dohnanyi 1969), with s being the size of a spherical grain. Our model yields a lower boundary of the size distribution $s_{\rm min} = 1.41^{+0.37}_{-0.21}$ μm and $q = 3.52 \pm 0.04$, with dust masses of $5.5^{+69.2}_{-0.4} \times 10^{-5} M_\oplus$ (inner belt) and $(4.6 \pm 0.2) \times 10^{-2} M_\oplus$ (outer belt). Although weakly constrained at $1.3^{+3.8}_{-1.1}$ au, the inner belt's location indicates that it should be markedly influenced by dynamical interactions with planets b and c (potentially carving Kirkwood-like gaps via large, resonant, eccentric increases; M. Yoshikawa 1989; J. Horner et al. 2020). MMR chains naturally arise from disk-driven planet migration, forming fragile ones for distant planets, especially around young stars (A. C. Petit et al. 2025). We tentatively conclude that dust grains are spatially segregated according to their size in the inner belt, whereas asteroids are concentrated on its outskirts. A sketch of the system architecture is shown in Figure 3.

5. Discussion

5.1. The Pair of Planets around HD 114082

O. V. Zakhozhay et al. (2022) adopted a one-planet Keplerian model to fit an RV curve affected by sparse irregular sampling and processing artifacts, yielding erroneous

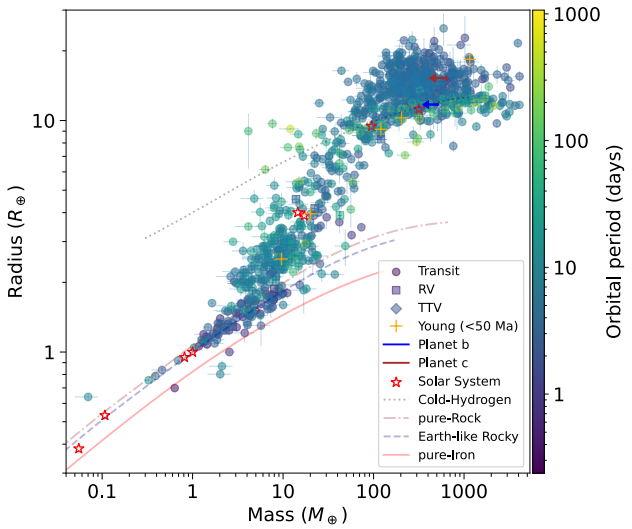

Figure 4. The R–M diagram with planets b and c (R and $M_{95\%}$ from Table 2), showing, as per the NASA Exoplanet Archive (J. L. Christiansen et al. 2025), planets discovered by the transit, RV, and TTV methods, with $\geqslant 3\sigma$ significant masses and radii; they are color-coded by orbital period, with crosses marking young cases (ages $\lesssim$50 Ma). Solar system planets are denoted by the red five-pointed stars. R–M relations for different compositions (L. Zeng et al. 2019) are shown as a reference.

parameters for planet b. FEROS data provide broad time coverage but show a high scatter, while the more precise HARPS data are clustered. We collected more public time-series spectra (spread over 6.2 yr), enhancing the data processing and markedly reducing the RV scatter. Using this refined dataset, our joint model yields a 95% confidence upper limit on the mass of planet b, which is one-fifth of planet b's value in O. V. Zakhozhay et al. (2022), while evidencing the errors in the orbital period and eccentricity therein.

Figure 4 shows the locations of planets b and c in the planetary radius versus mass diagram.

5.2. Formation and Evolution of the System

The observed properties of the HD 114082 system enable us to draw several inferences regarding its formation and evolution. The host star lies within the δ Scuti instability strip (O. V. Zakhozhay et al. 2022; A. Gautam et al. 2026) and above the Kraft break (R. P. Kraft 1967; A. C. Beyer & R. J. White 2024). With a predominantly radiative envelope and weak magnetic braking, the young star retains its primordial rotation and preserves any spin–orbit misalignment from planet migration or scattering. The almost coplanar, nearly circular orbits of the moderate-to-low-mass planets b and c, seemingly in near resonance and likely aligned with the inner dusty belt but inclined by $\sim 7^\circ$ to the outer exo-Kuiper Belt, favor the core accretion scenario for the planets' formation. The subsequent question is where it occurred.

Similar to the super-puff Kepler-51 d, which accreted and retains a substantial H/He envelope despite its small semimajor axis (Y. Tang et al. 2025), planets b and c could have formed in situ and grown to substantial sizes but limited masses. Alternatively, they could have emerged beyond the H_2O snow line (>5 au), from cores that were assembled in the protoplanetary disk and migrated inward into the observed orbits, while opening a gap in the debris disk. This migration could have been accelerated by tidal heating (inflated eccentric migration; H. Glanz et al. 2022), which could explain why these planets are so large for their masses.

The location of the high-albedo ($\sim$60%), low polarization ($\sim$17%) exo-Kuiper Belt could coincide with the CO_2 snow line (N. Engler et al. 2023). The vertical scale height of the outer belt in scattered light ($\leqslant$0.01; N. Engler et al. 2023) lies below the "minimum" expected level for a collisionally stirred disk (0.04 $\pm$ 0.02; P. Thébault 2009). This suggests that the outer belt is primordial and essentially undisturbed. By contrast, the inner planetesimal belt's dynamics must be driven by interaction with the pair of planets b and c. They likely have driven planetesimal orbits within the inner belt to the same inclination within the secular evolution timescale (e.g., M. C. Wyatt et al. 1999; A. A. Sefilian et al. 2025). Thus, our findings suggest that the inner belt is coplanar with the planetary orbits, having evolved together.

6. Conclusions

Follow-up observations and ancillary data enable us to study the multiplanet system around the F-type star HD 114082 with greater details and confidence. Orbital parameters, radii, and 95% confidence upper limits on the masses of planets b and c are fairly constrained. Thus, we yield an accurate and precise orbital period for planet b and majorly categorize planet c, advancing it toward confirmation—pending one more transit detection. In addition, we present a two-component model that accounts for the infrared excess from the inner asteroid belt and the exo-Kuiper Belt of HD 114082.

We highlight that planets b and c are the two longest-period known young transiting exoplanets. They are low-density giants with an orbital period ratio consistent with two commensurabilities, the MMRs 7:5 and 3:2. These planets have almost coplanar, circular orbits, misaligned with the outer, likely primordial exo-Kuiper Belt. They could have formed by core accretion and reached the observed orbits after migrating from the formation site, undergoing tidal heating while growing farther from the inner belt, clearing it all the way through and shelving it dynamically. Alternatively, these giants could be Neptune-mass planets that formed in situ and experienced a combination of boil-off and photoevaporative mass loss, as occurs for the super-puffs.

We intend to precisely determine the period of planet c and perform a full analysis of the TTVs from transit observations in the next years, aiming at further characterizing the system, including the determination of the planetary masses and the discernment of any resonance.

Acknowledgments

We thank the referee for providing useful comments. We thank the CHEOPS staff, in particular Bruno Merín (ESA CHEOPS Project Scientist for the Guest Observers program) for his guidance and devoted support. We are also grateful to Nikolaus Volgenau (Operations Scientist at LCO) for his kind support during the LCO Director's Discretionary Time preparation. C.d.B. acknowledges support from the Agencia Estatal de Investigación del Ministerio de Ciencia, Innovación y Universidades (MCIU/AEI) under grant WEAVE: EXPLORING THE COSMIC ORIGINAL SYMPHONY, FROM STARS TO GALAXY CLUSTERS and from the European Regional Development Fund (ERDF) with reference PID2023-153342NB-I00/10.13039/501100011033, as well as

from a Beatriz Galindo Senior Fellowship (BG22/00166) from the MICIU. The University of La Laguna (ULL) and the Department of Economy, Knowledge, and Employment of the Government of the Canary Islands are also gratefully acknowledged for the support provided to C.d.B. (2024/347). A.S.M. acknowledges financial support from the Spanish Ministry of Science and Innovation (MICINN) project PID2020-117493GB-I00 and from the Government of the Canary Islands project ProID2020010129. J.P.M. acknowledges support from the National Science and Technology Council of Taiwan under grant NSTC 112-2112-M-001-032-MY3. This research has made use of the SIMBAD database, operated at CDS, Strasbourg, France. E.G. gratefully acknowledges support from UK Research and Innovation (UKRI) under the UK government's Horizon Europe funding guarantee for an ERC Starting Grant (grant No. EP/Z000890/1), which funds M.P.B. J.S.J. gratefully acknowledges support from FONDECYT grant 1240738 and from the ANID BASAL project FB210003. CHEOPS is an ESA mission in partnership with Switzerland, with important contributions to the payload and the ground segment from Austria, Belgium, France, Germany, Hungary, Italy, Portugal, Spain, Sweden, and the United Kingdom. The CHEOPS Consortium would like to gratefully acknowledge the support received by all the agencies, offices, universities, and industries involved. Their flexibility and willingness to explore new approaches were essential to the success of this mission. The CHEOPS data analyzed in this Letter will be made available at the CHEOPS mission archive (https://cheops.unige.ch/archive_browser/). This Letter includes data collected with the TESS mission, obtained from the MAST data archive at the Space Telescope Science Institute (STScI). Funding for the TESS mission is provided by the NASA Explorer Program. STScI is operated by the Association of Universities for Research in Astronomy, Inc., under NASA contract NAS 5-26555. The TESS data analyzed here can be accessed via doi:10.17909/t9-nmc8-f686 (TESS Team 2021). This research has made use of the Astrophysics Data System, funded by NASA under Cooperative Agreement 80NSSC25M7105. This work has made use of data from the European Space Agency (ESA) mission Gaia (https://www.cosmos.esa.int/gaia), processed by the Gaia Data Processing and Analysis Consortium (DPAC; https://www.cosmos.esa.int/web/gaia/dpac/consortium). Funding for the DPAC has been provided by national institutions, in particular the institutions participating in the Gaia Multilateral Agreement. This work makes use of observations from the Las Cumbres Observatory global telescope network. Based on data collected under the NGTS project at the ESO La Silla Paranal Observatory. The NGTS facility is operated by the consortium institutes with support from the UK Science and Technology Facilities Council (STFC) under projects ST/M001962/1, ST/S002642/1, and ST/W003163/1. This work uses data obtained with the ASTEP+ telescope, at Concordia Station in Antarctica. ASTEP+ benefited from the support of the French and Italian polar agencies IPEV and PNRA in the framework of the Concordia station program and from OCA, INSU, Idex UCAJEDI (ANR-15-IDEX-01), and ESA through the Science Faculty of the European Space Research and Technology Centre (ESTEC). We also received funding via the Science and Technology Facilities Council (STFC; grant Nos. ST/S00193X/1, ST/W002582/1, and ST/Y001710/1), as well as from the European Research Council (ERC) under the European Union's Horizon 2020 research and innovation program (grant agreement No. 803193/BEBOP). We would like to acknowledge the dedicated staff of the French and Italian polar agencies (IPEV and PNRA) for their dedication and for their work, particularly those who overwinter, which is essential for keeping the Concordia Station operational throughout the austral winter, thanks to whom the ASTEP+ telescope could collect data for this publication. Based on data obtained from the ESO Science Archive Facility that can be accessed via doi:10.18727/archive/33 (European Southern Observatory (ESO) 2014), under programmes 0101.A-9012 and 113.26Y7.001 (PI: R. Launhardt), 0103.A-9010, 0107.A-9004, 0108.A-9014, and 0109.A-9014 (PI: O. Zakhozhay), and 098.C-0739 and 1101.C-0557 (PI: A. M. Lagrange). M.L. acknowledges the support of the Swiss National Science Foundation, grant PCEFP2_194576. The contributions of M.L. and H.P.O. have been carried out within the NCCR PlanetS supported by the Swiss National Science Foundation under grants 51NF40_182901 and 51NF40_205606. This publication makes use of the Data & Analysis Center for Exoplanets (DACE), which is a facility based at the University of Geneva (CH), dedicated to extrasolar planets' data visualization, exchange, and analysis. DACE is a platform of the Swiss National Centre of Competence in Research (NCCR) PlanetS, federating the Swiss expertise in Exoplanet research. The DACE platform is available at https://dace.unige.ch. This research has made use of the NASA Exoplanet Archive, which is operated by the California Institute of Technology, under contract with the National Aeronautics and Space Administration under the Exoplanet Exploration Program. The data used in this Letter can be accessed via doi:10.26133/NEA2 (Confirmed Planets Table; NASA Exoplanet Archive 2019).

Facilities: TESS, CHEOPS, NGTS, LCO, ESO:3.6m, Max Planck:2.2m..

Software: In addition to those mentioned explicitly in the text, this work has made use of the following software packages: ASTROPY (Astropy Collaboration et al. 2013, 2018, 2022), CORNER (D. Foreman-Mackey 2016), MATPLOTLIB (J. D. Hunter 2007), NUMPY (C. R. Harris et al. 2020), and SCIPY (P. Virtanen et al. 2020).

Author Contributions

C.d.B. was responsible for the idea, leading several successful observing proposals, coordinating the project, characterizing the star, computing TTVs, creating figures, contributing to the overall analysis, developing the full interpretation, and writing and submitting the manuscript. A.S.M. computed the RV measurements, built and performed the global photometric and RV model, created the related figures, and edited the manuscript. A.H. performed the LCO data reduction, contributed to the discussion on the nature of planet c, and edited the manuscript. J.P.M. implemented the two-component model, fitted the infrared excess, created a figure, and edited the manuscript. P.J.W. conducted the NGTS observing plan and data reduction and contributed to the manuscript editing. E.M.B. and S.G. contributed to the NGTS data reduction. J.F.F. developed the NGTS pipeline. D.R.A., M.P.B., E.G., and S.U.M. planned the NGTS observations. J.McC. operated NGTS. M.L. made comments on the manuscript. I.A., F.H., J.S.J., M.M., L.D.N., A.M.S.S., S.S., S.U., J.I.V., R.G.W. and D. B. are members of NGTS. H.P.O.

belongs to CHEOPS and made comments on the manuscript. T.G. and A.T. allocated the ASTEP observations. O.S. is responsible for the ASTEP photometric pipelines. M.B. was responsible for the maintenance of ASTEP at the Concordia Station. A.A. was in charge of the ASTEP operations. I.P. and M.J.H. conducted the CHEOPS GTO programmes. M.R.B. is a member of NGTS. L.A., P.B., G.D., and D.M. are members of ASTEP+.

Appendix A
Stellar Characterization

HD 114082 is currently the bluest spectral type star among those with young transiting exoplanets. We apply the Bayesian inference code of C. del Burgo & C. Allende Prieto (2016, 2018) on a grid of PARSEC 1.2S stellar evolution models (A. Bressan et al. 2012; Y. Chen et al. 2014, 2015; J. Tang et al. 2014) to derive the fundamental stellar parameters. The arranged grid of models comprises ages from 2 to 13,800 million years, with steps of 5%, and metallicities (M/H) from −2.18 to 0.51, with steps of 0.02 dex, adopting the photometric passband calibration of M. Riello et al. (2021) and the zero-points of the VEGAMAG system. The Bayesian code is fed by the absolute G magnitude M_G, the color G_{BP}–G_{RP} (Gaia Collaboration et al. 2023), and the stellar age (V. Squicciarini et al. 2025). Given the relatively small distance of the star, we assume null extinction when deriving G_{BP}–G_{RP} and M_G from Gaia DR3 photometry and astrometry. We estimated the stellar rotation period from the rotational broadening (vsini) value of O. V. Zakhozhay et al. (2022), assuming that HD 114082 is spinning in the plane of the likely primordial exo-Kuiper Belt (inclined by ≈83°; N. Engler et al. 2023). Table 3 shows the fundamental stellar parameters for our target.

A.1. Search for Stellar Companions

Using the Spectro-Polarimetric High-contrast Exoplanet REsearch at the Very Large Telescope, with an angular resolution of ≈25 mas, N. Engler et al. (2023) found only background stars within a $\lesssim 6\farcs5$ cone around the target, which they attributed to its proximity to the Galactic plane (latitude $\approx +2\fdg49$).

Table 3
Fundamental Stellar Parameters of HD 114082

Parameter	Value	References
Distance (pc)	95.06 ± 0.20	1
M_G (mag)	3.216 ± 0.005	1
BP–RP (mag)	0.568 ± 0.005	1
Age (Ma)	15 ± 3	2
Effective temperature (K)	6610 ± 23	3
Radius ($R_\odot$)	1.482 ± 0.021	3
Mass ($M_\odot$)	1.28 ± 0.07	3
Density (g cm^{-3})	0.55 ± 0.06	3
Surface gravity ($\log g$; cgs)	4.20 ± 0.03	3
Luminosity ($L_\odot$)	3.78 ± 0.07	3
Bolometric magnitude (mag)	3.297 ± 0.019	3
Iron-to-hydrogen abundance	−0.21 ± 0.25	3
vsini (km s^{-1})	39.2 ± 0.5	4
Rotational period (days)	1.85 ± 0.04	3

References. (1) Gaia Collaboration et al. (2023); (2) V. Squicciarini et al. (2025); (3) this work; and (4) O. V. Zakhozhay et al. (2022).

Appendix B
Planetary Characterization

Our global GP model, used for joint fitting, follows the equation below, with the relative flux ΔF in parts per thousand (ppt) and the relative RV ΔV_R in m s^{-1}:

$$\Delta F = Z_{F,j} + GP_j + PS_F,$$
$$\Delta V_R = Z_{V_R,j} + T_L + T_B + GP + PS_{V_R}, \quad \text{(B1)}$$

where PS_F is the planetary signal in the light curve, PS_{V_R} is the planetary signal in the RV curve, T_L is the linear trend, T_B is the trend against bisector span, and $Z_{F,j}$ and $Z_{V_R,j}$ represent the zero-points of each individual source of data (denoted by j), with the priors $\mathcal{N}[0, 5]$ ppt for ΔF and $\mathcal{N}[0, 1000]$ m s^{-1} for ΔV_R. T_L accounts for very long-term variations, with a prior $\mathcal{N}[0, 1000]$ m s^{-1} and BJD 2459332.9583 indicating the midpoint of the RV baseline.

In joint fitting to two-planet systems, PS_F constrains—per component—the planet-to-star-radius ratio (R/R_*), orbital period (P), eccentricity (e; primarily if secondary transits are observed), inclination (i), and scaled semimajor axis $a/R_\star$. The stellar density ($\rho_\star$) is robustly bounded from the ensemble of transit durations, even for moderately eccentric orbits. PS_{V_R}, in turn, constrains each planet's mass (given the stellar mass, $M_\star$), P, and e, provided the data have sufficient S/N and are well sampled. We use $\rho_\star$ and $M_\star$, together with the effective temperature, surface gravity, and iron-to-hydrogen abundance (Fe/H; which inform limb-darkening coefficients), as priors or to convert relative quantities into absolute planetary values.

Figures 5 and 6 respectively show the different light curves and the RV curve employed to perform our analysis, while Figure 7 illustrates the results from our joint modeling.

B.1. CCF Bisector Span

We identify a correlation between the RV measurements and the bisector span of the CCF. In particular, for the more precise HARPS data, we find a Spearman's rank correlation coefficient (C. Spearman 1904) of –0.59 (p-value <0.01). Previous RV surveys for stars above the Kraft break (e.g., A.-M. Lagrange et al. 2009), such as HD 114082 (see Section 2 and Section 5.2), have found correlations between the RV and bisector span to be a common result of stellar variability. We account for this effect by including linear terms between the RV and bisector span for the HARPS and FEROS data.

B.2. GP Modeling

We apply GP regression to model the short-term variability of stellar and instrumental origin. This flexible, probabilistic machine learning method defines a probability distribution over functions, employs a kernel to encode relationships between data points, and yields predictions with quantified uncertainty. For ground-based photometry, most variability arises from systematic effects and scintillation noise, which vary by data source. Each source is modeled independently with a simple harmonic oscillator (SHO) kernel (D. Foreman-Mackey et al. 2017). We rely on the same kernel for the RV data.

Here, the SHO kernel $k_{SHO}(\tau, \alpha_j, P_j, Q_j)$ depends on the time interval τ, the standard deviation of the process (α_j), the oscillator period (P_j), and the oscillator quality factor (Q_j),

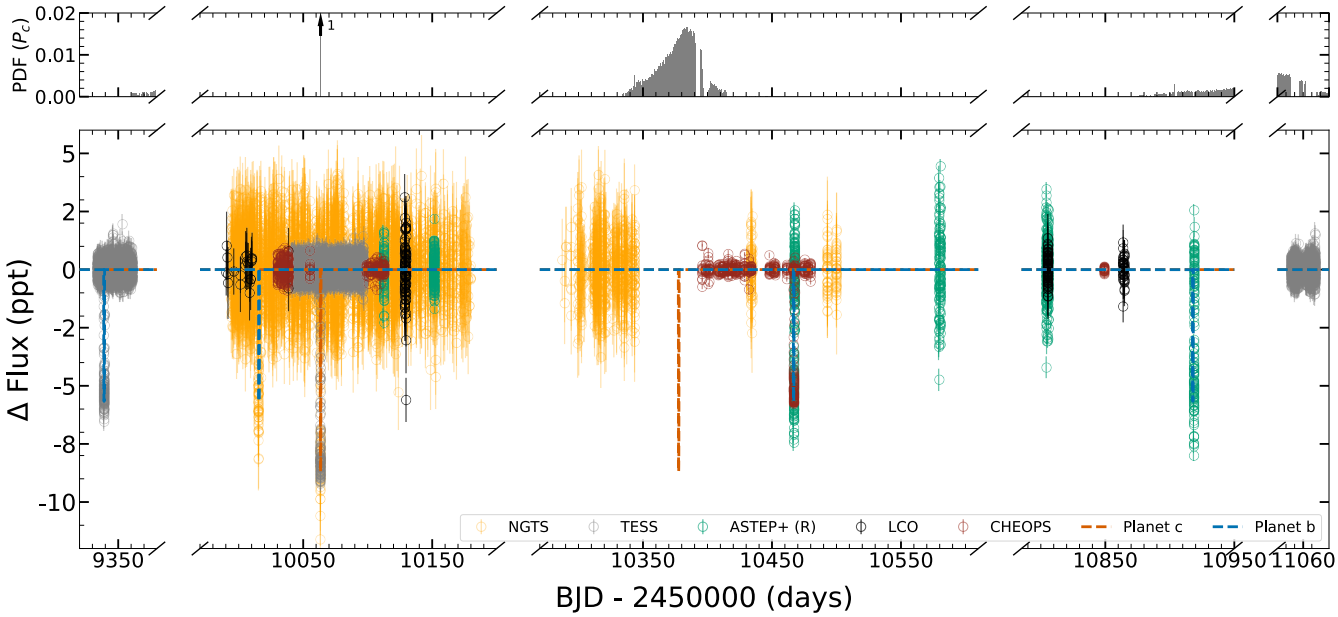

Figure 5. Top: PDF of midtransit times for planet c (12 hr bins; T_{14}= 13.21 hr). The PDF of the observed transit integrates to unity (BJD 246063.5112; $\sigma \approx$ 1.7 min $\lll$ bin width). Bottom: full photometric dataset, derived from different facilities, after detrending from stellar and instrumental effects. The data used to generate this figure are available in machine-readable format (see Figure 1).

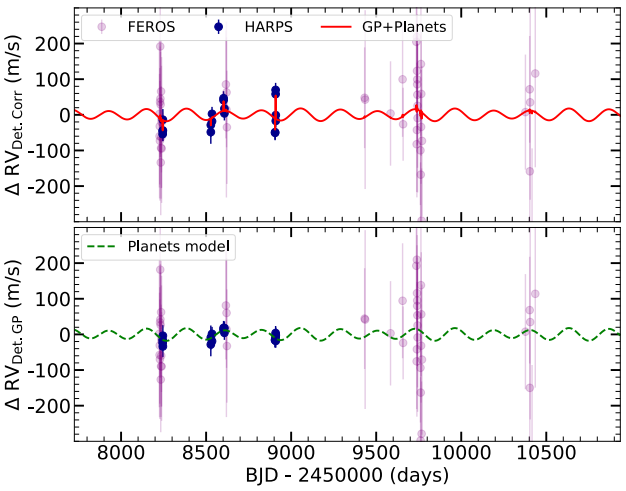

Figure 6. Top: RV curve, with HARPS and FEROS data points, after detrending from the long-term trend and the correlation with the bisector span. Bottom: RV curve detrended from the GP variations with the planetary model (PS_{V_R}). The data used to generate this figure are available in machine-readable format (see Figure 2).

related to the evolution timescale (L) as $Q = \frac{\pi L}{P_s}$, where P_s is the stellar variability period. For all parameters, log-uniform priors with values $\mathcal{U}[-10, 10]$ are used, to ensure that they are always positive and have the maximum flexibility.

B.3. Planetary Models

The transit signals are modeled using Pytransit (H. Parviainen 2015), with quadratic limb-darkening parameters derived from the Limb Darkening Toolkit (H. Parviainen & S. Aigrain 2015), while for RV signals, sinusoidal functions are employed. We optimize the orbital and physical parameters T_0, P, R, and b, and transform them into i, K, R/R_*, and $a/R_\star$, inside the likelihood, using as priors the aforementioned stellar

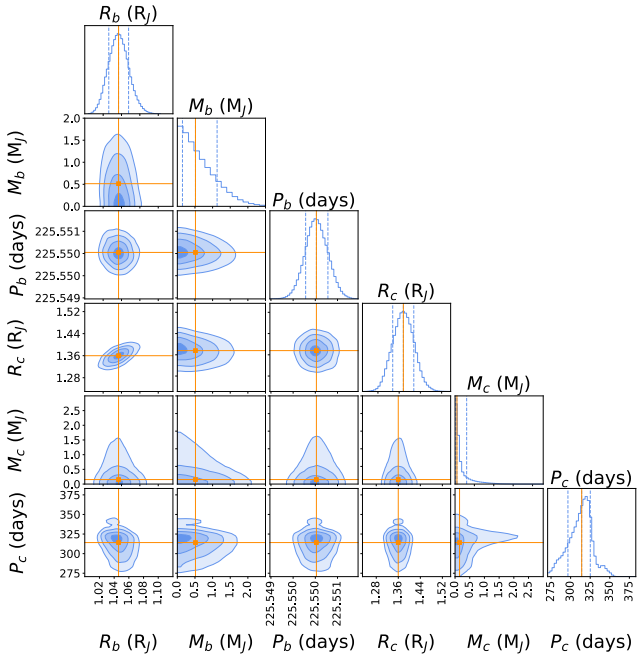

Figure 7. Corner plot of the parameters from the best joint model fit: correlation maps and posterior distributions.

parameters, listed in Appendix A. The optimization process implicitly performs an end-to-end uncertainty propagation. For T_0, we use the prior $\mathcal{N}[T0, 0.1]$ (days), introducing the known transit epochs. For P, we apply the prior $\mathcal{LU}[20, 8000]$ (days). For R, we use $\mathcal{LU}[0.007, 2.7]$ (R_J), and for M, we use $\mathcal{LU}[0.007, 20]$ (M_J). For b, a uniform prior $\mathcal{U}[0, 1.2]$ is applied, allowing for grazing transits and even nontransiting solutions. In the case of TESS data, we include a dilution parameter $\mathcal{N}[1.0, 0.3]$.

In order to test circular and eccentric models, we adopt a parameterization that separates the eccentricity e and the

argument of periapsis ω into $x = \sqrt{e}\cos\omega$ and $y = \sqrt{e}\sin\omega$, applying a normal prior $\mathcal{N}[0, 0.3]$ on both components of the eccentricity vector. The (e, ω) parameterization induces strong covariance at low e, due to rotational degeneracy in the likelihood, while the adopted vector maps the parameter space to the unit disk, removes the (e, ω) covariance ridge at $e \to 0$, and allows ω to be undefined at $e = 0$ without sampling artifacts. The independent normal priors $\mathcal{N}(0, 0.3)$ on x and y induce a smooth $\propto\sqrt{e}$ prior on e—weakly informative and well suited for Bayesian model selection. This parameterization yields a distribution of eccentricities similar to that proposed by D. M. Kipping (2013), based on the distribution of eccentricities of known planets. Thus, it avoids any statistical issue that occurs when trying to fit simultaneously the correlated e and ω from a single constraint like the transit duration. The inferred eccentricities of both planets are consistent with zero ($e_b < 0.2$, $e_c < 0.3$), with Bayesian evidence favoring the circular model (see Table 6). However, we cannot rule out low but nonzero eccentricities.

B.4. White-noise Terms

Finally, we include white-noise terms for all data sources, to account for possible unmodeled variability. We adopt a prior $\mathcal{LU}[0.007, 150]$ ppt for all photometric sources and a prior $\mathcal{LU}[5^{-5}, 22000]$ m s^{-1} for RV data.

Appendix C
TTVs

REBOUND (H. Rein & S. F. Liu 2012; H. Rein & D. S. Spiegel 2015) is an N-body integrator that enables us to assess the TTVs on planet b induced by its planetary companion. Adopting the respective masses of 1.6 and 2.0 M_J for planets b and c—i.e., the values of the 95% confidence upper limits listed in Table 2—the resulting TTV semiamplitude (determined from all virtual midtransit times in the time span between the first and last observed transits) is nearly 2 hr (95% confidence limit), rejecting the candidate period $P_{1/2}$ of about 112.78 days for planet b from our alias testing observations, as a dip would have been recorded (see Figure 1).

The transit duration of planet b—the same at two observing epochs, from TESS and CHEOPS—is fixed to derive the midtransit times of partial (∼50% coverage) NGTS and ASTEP+ transits. The four measures enable us to estimate a TTV semiamplitude of $\lesssim 4 \pm 2$ hr for planet b; this far exceeds any conceivable midtransit time jitter and suggests a planet c mass significantly smaller than that of Jupiter, particularly if the pair is locked in an MMR. Given the small statistics, instead of directly including the TTVs in our joint modeling, to further constrain the planetary masses, we choose to refine them subsequently. After feeding REBOUND with approximately 1 million representations that settle the full posterior distributions of the parameters for the preferred circular solution shown in Tables 2 and 6, those producing TTVs greater than the conservative value of 10 hr are filtered out. As a result, $M_{95\%}$ for planets b and c decrease from 1.6 and 2.0 M_J to 1.5 and 0.24 M_J, respectively, yielding a TTV semiamplitude on planet b of about 7 hr (95% confidence limit).

Appendix D
Nature of Planet C

Planet c's transit, fully observed by TESS and with the same depth and >50% coverage by NGTS, cannot be an artifact. Moreover, the RV curve imposes upper limits for its planetary mass (as it does for planet b), and the debris disk fences off its location, with an inclination between the plane of the exo-Kuiper Belt and those of the planetary orbits. This evidence strongly supports planet c as a dynamically interacting body. In addition to ruling out stellar companions in Appendix A, a false-positive analysis is conducted here. Using TRICERATOPS (S. Giacalone et al. 2021), we find that none of the Gaia DR3 Catalogue stars (Gaia Collaboration et al. 2023) within the TESS aperture can affect or cause this transit, and rule out it being due to an unresolved eclipsing binary, by comparing its expected shape with that of the observed transit. Furthermore, Gaia DR3 yields a renormalized unit weight error of 0.944, signifying that HD 114082 is a single star.

Appendix E
System Architecture Modeling

Our model uses the 1D analytical radiative transfer code ARTIFACT (J. P. Marshall et al. 2023), exploring the parameter space using EMCEE (D. Foreman-Mackey et al. 2013). The adopted disk architecture consists of a pair of Gaussian belts, each defined by a peak radius and width. The radius and width of the cold belt are fixed at the ALMA-observed values ($r_{\rm cold} = 38$ au and FWHM $\leqslant 40$ au) from L. Matrà et al. (2025). A prior $\mathcal{N}[0.1, 10]$ au for the warm-belt radius ($r_{\rm warm}$) is applied, with a fixed fractional width of 0.1. Note the dust emission profile is dominated by the stellocentric radius rather than the belt width for symmetric architectures, such that the value of this parameter is somewhat arbitrary. For simplicity, we adopt a single power-law size distribution ($s_{\rm min}$, q) up to 3 mm and the same dust composition (astronomical silicate–astrosil; B. T. Draine 2003) for both belts, with each component's dust mass as a free parameter.

We sample the posterior with 60 walkers (10 per free parameter, including a nuisance factor) over 2000 steps each. Walkers are initialized uniformly between prior bounds. Namely, $\mathcal{N}[2, 5]$ for q, $\mathcal{N}[-2, 2]$ in $\log_{10}(\mu m)$ for $s_{\rm min}$, $\mathcal{N}[-1, 1]$ in $\log_{10}$(au) for $r_{\rm warm}$, and $\mathcal{N}[-6, 0]$ in $\log_{10}(M_\oplus)$ for the dust masses. Each realization of the disk model is compared to observed data points using error-weighted least-squares fitting. Posteriors are sampled from the final model realizations. Maximum amplitude probability values and associated uncertainties are obtained from the 16th, 50th, and 84th percentiles of the marginalized posteriors.

Appendix F
Additional Tables

Tables 4 and 5 provide relevant information about the CHEOPS and LCO observing campaigns, respectively. Table 6 shows the full set of priors and optimized values for the adopted circular model and the eccentric model.

Table 4
Information about the Individual CHEOPS Observing Campaigns, Including the Midtime, Duration (ΔT), and File Identification

Midtime BJD2450000	ΔT (hr)	File Key
10030.2669869135	3.20	PR100017_TG005901
10030.5503222360	2.93	PR100017_TG001301
10031.7926661754	1.41	PR100017_TG001701
10032.6871276520	4.47	PR100017_TG005401
10033.0690723600	2.27	PR100017_TG001901
10033.6774027506	1.06	PR100017_TG002001
10033.8829572285	1.07	PR100017_TG002101
10034.4348098873	4.09	PR100017_TG002201
10035.1503247325	5.26	PR100017_TG004901
10035.8058705040	1.06	PR100017_TG002501
10036.9732405210	1.06	PR100017_TG002701
10037.4662834690	1.45	PR100017_TG002801
10037.7454614015	3.20	PR100017_TG004401
10038.0287940680	4.95	PR100017_TG002901
10038.4537943546	5.05	PR100017_TG003001
10038.9183782640	1.55	PR100017_TG003201
10040.3030992053	3.20	PR100017_TG003901
10040.8176759845	2.71	PR100017_TG003801
10041.5482439375	4.56	PR100017_TG003701
10055.3468564620	1.55	PR100017_TG006201
10069.2429013816	1.01	PR100017_TG006401
10098.8371326667	0.70	PR100017_TG007001
10100.1037635445	1.55	PR100017_TG010401
10100.5532800066	2.10	PR100017_TG010501
10101.0343075204	0.71	PR100017_TG007901
10101.5148633397	0.92	PR100017_TG010701
10102.3641785895	1.98	PR100017_TG008101
10102.8190290960	0.72	PR100017_TG008201
10103.9218180776	3.41	PR100017_TG008401
10105.2912536770	2.57	PR100017_TG008701
10105.4287548630	0.92	PR100017_TG011501
10106.7329211803	0.92	PR100017_TG009001
10107.0148753454	4.03	PR100017_TG013601
10108.1755002120	0.91	PR100017_TG009301
10109.3002906220	1.71	PR100017_TG009501
10109.7548877370	3.96	PR100017_TG014201
10110.3725049040	2.56	PR100017_TG014301
10111.0864045927	3.21	PR100017_TG014401
10112.6440422570	3.42	PR100017_TG011801
10395.8878197840	1.06	PR140079_TG022501
10398.5037984470	1.54	PR140079_TG022502
10400.4774037595	1.06	PR140079_TG022503
10401.5051822490	1.06	PR140079_TG022601
10408.3003134946	1.41	PR140079_TG020501
10409.6642101766	1.54	PR140079_TG023101
10411.4642164180	1.54	PR140079_TG020502
10412.6044952828	1.54	PR140079_TG020503
10415.8989391990	3.91	PR140079_TG023301
10416.7121263184	1.06	PR140079_TG023001
10417.8086503630	1.06	PR140079_TG023102
10418.8072608896	1.44	PR140079_TG023002
10421.1651356560	3.32	PR140079_TG023401
10422.2611943750	1.05	PR140079_TG024101
10424.8642106615	0.99	PR140079_TG024001
10428.6378258370	2.45	PR140079_TG024102
10432.0301935254	1.54	PR140079_TG024002
10433.7239370504	3.19	PR140079_TG024401
10435.0718401910	1.00	PR140079_TG024201
10435.7199955634	3.19	PR140079_TG025401
10436.5519513395	1.54	PR140079_TG025601
10439.8674448620	0.99	PR140079_TG025701
10442.5672145397	3.19	PR140079_TG025801
10445.8561101425	1.54	PR140079_TG025602
10447.8419948937	3.19	PR140079_TG025802
10451.3088705390	3.22	PR140079_TG026001
10452.4276334317	1.54	PR140079_TG026002
10457.0632674615	1.86	PR140079_TG026201
10461.2736957060	1.82	PR140079_TG026202
10463.1604902204	4.01	PR140079_TG026301
10466.0370702036	46.96	PR240025_TG000301
10468.4345744494	1.82	PR140079_TG027501
10472.1338792680	1.61	PR140079_TG027601
10475.1049446850	3.58	PR140079_TG027401
10476.8611839170	3.28	PR140079_TG027402
10477.6461603073	1.63	PR140079_TG027602
10479.6690668985	0.90	PR140079_TG027502
10834.8044083250	3.55	PR250012_TG000201
10836.0448931560	5.67	PR240025_TG000601
10837.4745472097	2.58	PR250012_TG000202
10840.5773606063	2.05	PR240025_TG000501
10842.4855177826	3.90	PR240025_TG000602
10845.9837828200	2.09	PR240025_TG000603
10848.7252775384	3.02	PR240025_TG000604
10848.9342827920	4.43	PR250012_TG000203

Table 5
Detailed Information about the Individual LCO Observing Campaigns

Date	Site	Telescope	Filter	Exposure Time (s)	Cadence (s)	Duration (hr)	Program ID
25/12/2022	Siding Spring	0m4-03	rp	4.2	35.1	0.01	KEY2020B-007
26/12/2022	Siding Spring	0m4-03	rp	4.2	17.9	0.01	KEY2020B-007
15/02/2023	Siding Spring	0m4-03	zs	15.2	29.4	0.09	DDT2022B-007
16/02/2023	Siding Spring	0m4-03	zs	15.2	29.5	0.09	DDT2022B-007
05/03/2023	Siding Spring	0m4-05	V	15.3	29.5	0.109	DDT2022B-007
06/03/2023	Siding Spring	0m4-05	V	15.3	29.4	0.106	DDT2022B-007
07/03/2023	Siding Spring	0m4-05	V	15.3	29.5	0.11	DDT2022B-007
02/04/2023	Siding Spring	0m4-03	rp	4.3	18.4	0.01	KEY2020B-007
04/04/2023	Siding Spring	0m4-03	rp	4.3	18.6	0.01	KEY2020B-007
16/12/2022	Cerro Tololo	0m4-09	rp	4.3	17	0.01	KEY2020B-007
20/12/2022	Cerro Tololo	0m4-09	rp	4.3	17.1	0.01	KEY2020B-007
15/01/2023	Cerro Tololo	0m4-09	rp	4.3	36	0.01	KEY2020B-007
16/01/2023	Cerro Tololo	0m4-09	rp	4.3	17.2	0.01	KEY2020B-007
27/01/2023	Cerro Tololo	0m4-09	rp	4.3	17.3	0.01	KEY2020B-007
28/01/2023	Cerro Tololo	0m4-09	rp	4.3	17.2	0.01	KEY2020B-007
14/02/2023	Cerro Tololo	0m4-09	zs	15.3	28.8	0.089	DDT2022B-007
15/02/2023	Cerro Tololo	0m4-09	zs	15.3	28.1	0.087	DDT2022B-007
16/02/2023	Cerro Tololo	0m4-09	zs	15.3	28.3	0.086	DDT2022B-007
21/02/2023	Cerro Tololo	0m4-09	zs	15.3	28.3	0.087	DDT2022B-007
24/02/2023	Cerro Tololo	0m4-09	V	20.3	33.1	0.028	DDT2022B-007
26/02/2023	Cerro Tololo	0m4-09	V	20.4	33.2	0.101	DDT2022B-007
02/03/2023	Cerro Tololo	0m4-09	V	15.4	29.3	0.103	DDT2022B-007
03/03/2023	Cerro Tololo	0m4-09	V	15.3	30.9	0.104	DDT2022B-007
04/03/2023	Cerro Tololo	0m4-09	V	15.3	30.9	0.103	DDT2022B-007
05/03/2023	Cerro Tololo	0m4-09	V	15.3	30.9	0.103	DDT2022B-007
06/03/2023	Cerro Tololo	0m4-09	V	15.3	32.3	0.104	DDT2022B-007
07/03/2023	Cerro Tololo	0m4-09	V	15.3	30.7	0.104	DDT2022B-007
20/01/2023	Cerro Tololo	0m4-12	rp	4.2	12.7	0.007	KEY2020B-007
21/01/2023	Cerro Tololo	0m4-12	rp	4.2	13.2	0.007	KEY2020B-007
02/07/2023	Cerro Tololo	0m4-12	V	20.2	28.5	3.733	DDT2022B-007
03/07/2023	Cerro Tololo	0m4-12	V	20.2	28.5	3.48	DDT2022B-007
09/05/2025	Cerro Tololo	0m4-92	V	2	13.7	6.773	DDT2025A-006
06/07/2025	Cerro Tololo	0m4-92	V	2	4.6	1.943	DDT2025A-006
07/07/2025	Cerro Tololo	0m4-92	V	2	4.4	1.965	DDT2025A-006

Table 6
Full Set of Priors and Optimized Values for the Adopted Circular Model and the Eccentric Model

Parameter	Prior	Value (Circular Model)	Value (Eccentric Model)
White noise			
ln $\sigma F_{\rm TESS}$ [ppt]	$\mathcal{U}[-5,5]$	<–4.5	<–4.7
ln $\sigma F_{\rm NGTS}$ [ppt]	$\mathcal{U}[-5,5]$	<–3.1	<–2.9
ln $\sigma F_{\rm CHEOPS}$ [ppt]	$\mathcal{U}[-5,5]$	-1.37 ± 0.04	-1.38 ± 0.05
ln $\sigma F_{\rm ASTEP+}$ [ppt]	$\mathcal{U}[-5,5]$	0.082 ± 0.024	0.074 ± 0.025
ln $\sigma F_{\rm LCO}$ [ppt]	$\mathcal{U}[-5,5]$	-0.04 ± 0.016	-0.055 ± 0.011
ln $\sigma RV_{\rm HARPS}$ [m· s^{-1}]	$\mathcal{U}[-10,10]$	<1.9	<1.9
ln $\sigma RV_{\rm FEROS}$ [m· s^{-1}]	$\mathcal{U}[-10,10]$	<2.8	<3.0
Zero-points			
V0 $F_{\rm TESS}$ [ppt]	$\mathcal{N}[0,5]$	0.03 ± 0.03	0.03 ± 0.03
V0 $F_{\rm NGTS}$ [ppt]	$\mathcal{N}[0,5]$	-0.07 ± 0.017	$-0.03^{+0.17}_{-0.18}$
V0 $F_{\rm CHEOPS}$ [ppt]	$\mathcal{N}[0,5]$	0.081 ± 0.019	0.071 ± 0.019
V0 $F_{\rm ASTEP+}$ [ppt]	$\mathcal{N}[0,5]$	0.5 ± 0.4	0.4 ± 0.4
V0 $F_{\rm LCO}$ [ppt]	$\mathcal{N}[0,5]$	-0.15 ± 0.15	0.0 ± 0.4
V0 $RV_{\rm HARPS}$ [m· s^{-1}]	$\mathcal{N}[0,1000]$	21^{+26}_{-24}	25^{+24}_{-27}
V0 $RV_{\rm FEROS}$ [m· s^{-1}]	$\mathcal{N}[0,1000]$	6^{+24}_{-25}	4^{+23}_{-24}
Polynomial and correlations			
Lin RV [m· s^{-1}· $days^{-1}$]	$\mathcal{N}[0,100]$	0.02 ± 0.03	0.03 ± 0.03
Lin $RV - BIS_{\rm HARPS}$	$\mathcal{N}[0,100]$	-0.11 ± 0.04	-0.12 ± 0.04
Lin $RV - BIS_{\rm FEROS}$	$\mathcal{N}[0,100]$	-0.012 ± 0.014	-0.010 ± 0.016
GP hyperparameters			
ln $\sigma F_{\rm TESS}$ [ppt]	$\mathcal{U}[-10,10]$	-1.06 ± 0.05	-1.08 ± 0.06
ln $PF_{\rm TESS}$ [days]	$\mathcal{U}[-10,10]$	0.25 ± 0.05	0.23 ± 0.06
ln $TsF_{\rm TESS}$ [days]	$\mathcal{U}[-10,10]$	-1.66 ± 0.09	-1.69 ± 0.11
ln $\sigma F_{\rm NGTS}$ [ppt]	$\mathcal{U}[-10,10]$	0.48 ± 0.06	0.47 ± 0.07
ln $PF_{\rm NGTS}$ [days]	$\mathcal{U}[-10,10]$	$0.14^{+0.19}_{-0.16}$	$0.16^{+0.15}_{-0.19}$
ln $TsF_{\rm NGTS}$ [days]	$\mathcal{U}[-10,10]$	$-3.2^{+0.4}_{-0.3}$	$-3.0^{+0.3}_{-0.4}$
ln $\sigma F_{\rm CHEOPS}$ [ppt]	$\mathcal{U}[-10,10]$	-0.99 ± 0.04	-1.00 ± 0.04
ln $PF_{\rm CHEOPS}$ [days]	$\mathcal{U}[-10,10]$	-3.51 ± 0.08	$-3.48^{+0.08}_{-0.09}$
ln $TsF_{\rm CHEOPS}$ [days]	$\mathcal{U}[-10,10]$	$-4.76^{+0.24}_{-0.23}$	-4.66 ± 0.25
ln $\sigma F_{\rm ASTEP+}$ [ppt]	$\mathcal{U}[-10,10]$	$0.56^{+0.10}_{-0.11}$	$0.60^{+0.15}_{-0.11}$
ln $PF_{\rm ASTEP+}$ [days]	$\mathcal{U}[-10,10]$	$-2.7^{+0.7}_{-0.5}$	$-3.3^{+0.9}_{-0.8}$
ln $TsF_{\rm ASTEP+}$ [days]	$\mathcal{U}[-10,10]$	$-6.5^{+1.4}_{-1.0}$	$-7.8^{+1.7}_{-1.5}$
ln $\sigma F_{\rm LCO}$ [ppt]	$\mathcal{U}[-10,10]$	$1.21^{+0.12}_{-0.13}$	1.04 ± 0.18
ln $PF_{\rm LCO}$ [days]	$\mathcal{U}[-10,10]$	$-7.06^{+0.10}_{-0.22}$	$-1.9^{+0.4}_{-0.8}$
ln $TsF_{\rm LCO}$ [days]	$\mathcal{U}[-10,10]$	$-1.1^{+0.5}_{-0.4}$	$-4.8^{+3.6}_{-2.0}$
ln σ RV [m· s^{-1}]	$\mathcal{U}[-10,10]$	3.6 ± 0.3	3.6 ± 0.4
ln PRV [days]	$\mathcal{U}[-10,10]$	$-0.7^{+2.0}_{-1.7}$	$-0.4^{+2.0}_{-1.9}$
ln $TsRV$ [days]	$\mathcal{U}[-10,10]$	-3 ± 4	1 ± 6
Stellar parameters			
R_* [$R_\odot$]	$\mathcal{N}[1.482,0.021]$	1.473 ± 0.014	1.479 ± 0.018
M_* [$M_\odot$]	$\mathcal{N}[1.28,0.07]$	1.31 ± 0.04	1.31 ± 0.06
Limb darkening			
q1	$\mathcal{N}[0.240,0.014]$	0.242 ± 0.011	0.239 ± 0.013
q2	$\mathcal{N}[0.265,0.019]$	0.263 ± 0.014	0.262 ± 0.017
Dilution parameters			
$D_{\rm TESS}$	$\mathcal{N}[1.0, 0.3]$	1.08 ± 0.03	1.10 ± 0.03
Planet b (circular)			
$T0$ [BJD—2450000]	$\mathcal{N}[10466.8,0.1]$	10466.7908 ± 0.0017	$10466.7911^{+0.0016}_{-0.0020}$
ln P [days]	$\mathcal{U}[3,9]$	$5.4185442 \pm 1.8\times10^{-6}$	$5.4185455 \pm 1.9\times10^{-6}$
ln $R_{\rm p}$ [$R_{\rm J}$]	$\mathcal{U}[-5,1]$	0.045 ± 0.013	0.047 ± 0.016
ln $M_{\rm p}$ [$M_{\rm J}$]	$\mathcal{U}[-5,3]$	<0.5	<0.28
b	$\mathcal{U}[0,1.2]$	$0.421^{+0.022}_{-0.024}$	$0.36^{+0.08}_{-0.12}$
$\sqrt{e}\cos\omega$	$\mathcal{N}[0,0.3]$	0 (fixed)	$-0.04^{+0.26}_{-0.25}$
$\sqrt{e}\sin\omega$	$\mathcal{N}[0,0.3]$	0 (fixed)	$-0.11^{+0.12}_{-0.15}$
Planet c (circular)			
$T0$ [BJD—2450000]	$\mathcal{N}[10063.5,0.1]$	10063.5114 ± 0.0009	10063.5111 ± 0.0011
ln P [days]	$\mathcal{U}[3,9]$	$5.75^{+0.035}_{-0.058}$	$5.84^{+0.48}_{-0.17}$
ln $R_{\rm p}$ [$R_{\rm J}$]	$\mathcal{U}[-5,1]$	$0.307^{+0.018}_{-0.019}$	0.316 ± 0.022
ln $M_{\rm p}$ [$M_{\rm J}$]	$\mathcal{U}[-5,3]$	<0.7	<0.7
b	$\mathcal{U}[0,1.2]$	$0.752^{+0.009}_{-0.008}$	0.753 ± 0.011

Table 6
(Continued)

Parameter	Prior	Value (Circular Model)	Value (Eccentric Model)
$\sqrt{e}\cos\omega$	$\mathcal{N}[0,0.3]$	0 (fixed)	$0.04^{+0.26}_{-0.29}$
$\sqrt{e}\sin\omega$	$\mathcal{N}[0,0.3]$	0 (fixed)	$0.11^{+0.27}_{-0.20}$
$\ln Z$		−23,693.1	−23,698.4

Note. Uncertainties are 1σ. The limits show the 95% confidence interval.

ORCID iDs

Carlos del Burgo https://orcid.org/0000-0002-8949-5200
Alejandro Suárez Mascareño https://orcid.org/0000-0002-3814-5323
Ana Heras https://orcid.org/0000-0002-6342-9600
Jonathan P. Marshall https://orcid.org/0000-0001-6208-1801
Peter J. Wheatley https://orcid.org/0000-0003-1452-2240
Edward M. Bryant https://orcid.org/0000-0001-7904-4441
Samuel Gill https://orcid.org/0000-0002-4259-0155
Jorge Fernández Fernández https://orcid.org/0000-0002-1416-2188
David R. Anderson https://orcid.org/0000-0001-7416-7522
Matthew P. Battley https://orcid.org/0000-0002-1357-9774
Edward Gillen https://orcid.org/0000-0003-2851-3070
Solène Ulmer-Moll https://orcid.org/0000-0003-2417-7006
James McCormac https://orcid.org/0000-0003-1631-4170
Monika Lendl https://orcid.org/0000-0001-9699-1459
Ioannis Apergis https://orcid.org/0009-0004-7473-4573
Faith Hawthorn https://orcid.org/0000-0002-8675-182X
James S. Jenkins https://orcid.org/0000-0003-2733-8725
Maximiliano Moyano https://orcid.org/0000-0002-7927-9555
Louise D. Nielsen https://orcid.org/0000-0002-5254-2499
Alexis M. S. Smith https://orcid.org/0000-0002-2386-4341
Suman Saha https://orcid.org/0000-0001-8018-0264
Stéphane Udry https://orcid.org/0000-0001-7576-6236
Jose I. Vines https://orcid.org/0000-0002-1896-2377
Richard G. West https://orcid.org/0000-0001-6604-5533
Daniel Bayliss https://orcid.org/0000-0001-6023-1335
Hugh P. Osborn https://orcid.org/0000-0002-4047-4724
Tristan Guillot https://orcid.org/0000-0002-7188-8428
Amaury H. M. J. Triaud https://orcid.org/0000-0002-5510-8751
Olga Suarez https://orcid.org/0000-0002-3503-3617
Matteo Beltrame https://orcid.org/0009-0006-2606-3271
Abdelkrim Agabi https://orcid.org/0000-0001-7948-6493
Isabella Pagano https://orcid.org/0000-0001-9573-4928
Matthew J. Hooton https://orcid.org/0000-0003-0030-332X
Matthew R. Burleigh https://orcid.org/0000-0003-0684-7803
Lyu Abe https://orcid.org/0000-0002-0856-4527
Philippe Bendjoya https://orcid.org/0000-0002-4278-1437
Georgina Dransfield https://orcid.org/0000-0002-3937-630X
Djamel Mékarnia https://orcid.org/0000-0001-5000-7292

References

Armitage, P. J. 2024, arXiv:2412.11064
Astropy Collaboration, Price-Whelan, A. M., Lim, P. L., et al. 2022, ApJ, 935, 167
Astropy Collaboration, Price-Whelan, A. M., Sipőcz, B. M., et al. 2018, AJ, 156, 123
Astropy Collaboration, Robitaille, T. P., Tollerud, E. J., et al. 2013, A&A, 558, A33
Avallone, E. A., Tayar, J. N., van Saders, J. L., et al. 2022, ApJ, 930, 7
Baranne, A., Queloz, D., Mayor, M., et al. 1996, A&AS, 119, 373
Barragán, O., Yu, H., Freckelton, A. V., et al. 2024, MNRAS, 531, 4275
Benatti, S., Damasso, M., Borsa, F., et al. 2021, A&A, 650, A66
Benz, W., Broeg, C., Fortier, A., et al. 2021, ExA, 51, 109
Bergez-Casalou, C., Bitsch, B., & Raymond, S. N. 2023, A&A, 669, A129
Bergez-Casalou, C., & Kral, Q. 2024, A&A, 692, A156
Best, M., Sefilian, A. A., & Petrovich, C. 2024, ApJ, 960, 89
Beyer, A. C., & White, R. J. 2024, ApJ, 973, 28
Bressan, A., Marigo, P., Girardi, L., et al. 2012, MNRAS, 427, 127
Broeg, C., Fernández, M., & Neuhäuser, R. 2005, AN, 326, 134
Brown, T. M., Baliber, N., Bianco, F. B., et al. 2013, PASP, 125, 1031
Caldwell, D. A., Tenenbaum, P., Twicken, J. D., et al. 2020, RNAAS, 4, 201
Carrera, D., Raymond, S. N., & Davies, M. B. 2019, A&A, 629, L7
Chen, C. H., Mittal, T., Kuchner, M., et al. 2014, ApJS, 211, 25
Chen, Y., Bressan, A., Girardi, L., et al. 2015, MNRAS, 452, 1068
Chen, Y., Girardi, L., Bressan, A., et al. 2014, MNRAS, 444, 2525
Christiansen, J. L., McElroy, D. L., Harbut, M., et al. 2025, PSJ, 6, 186
Crouzet, N., Agabi, A., Guillot, T., et al. 2020, SPIE, 11447, 114470O
del Burgo, C., & Allende Prieto, C. 2016, MNRAS, 463, 1400
del Burgo, C., & Allende Prieto, C. 2018, MNRAS, 479, 1953
Delisle, J. B., Unger, N., Hara, N. C., & Ségransan, D. 2022, A&A, 659, A182
Dohnanyi, J. S. 1969, JGR, 74, 2531
Draine, B. T. 2003, ApJ, 598, 1017
Dransfield, G., Mékarnia, D., Triaud, A. H. M. J., et al. 2022, SPIE, 12186, 121861F
Drążkowska, J., Bitsch, B., Lambrechts, M., et al. 2023, ASPC, 534, 717
Engler, N., Milli, J., Gratton, R., et al. 2023, A&A, 672, A1
European Southern Observatory (ESO) 2014, HARPS reduced data obtained by standard ESO pipeline processing, European Southern Observatory (ESO), doi:10.18727/ARCHIVE/33
Fellgett, P. 1955, AcOpt, 2, 9
Foreman-Mackey, D. 2016, JOSS, 1, 24
Foreman-Mackey, D., Agol, E., Ambikasaran, S., & Angus, R. 2017, AJ, 154, 220
Foreman-Mackey, D., Hogg, D. W., Lang, D., & Goodman, J. 2013, PASP, 125, 306
Fulton, B. J., Rosenthal, L. J., Hirsch, L. A., et al. 2021, ApJS, 255, 14
Gagné, J., Mamajek, E. E., Malo, L., et al. 2018, ApJ, 856, 23
Gaia Collaboration, Prusti, T., de Bruijne, J. H. J., et al. 2016, A&A, 595, A1
Gaia Collaboration, Vallenari, A., Brown, A. G. A., et al. 2023, A&A, 674, A1
García, R. A., Gourvès, C., Santos, A. R. G., et al. 2023, A&A, 679, L12
Gautam, A., Murphy, S. J., & Bedding, T. R. 2026, MNRAS, 545, staf2001
Giacalone, S., Dressing, C. D., Jensen, E. L. N., et al. 2021, AJ, 161, 24
Glanz, H., Rozner, M., Perets, H. B., & Grishin, E. 2022, ApJ, 931, 11
Harris, C. R., Millman, K. J., van der Walt, S. J., et al. 2020, Natur, 585, 357
Hasegawa, Y., Haworth, T. J., Hoadley, K., et al. 2022, ApJL, 926, L23
Hauschildt, P. H., Allard, F., & Baron, E. 1999, ApJ, 512, 377
Helled, R. 2023, A&A, 675, L8
Høg, E., Fabricius, C., Makarov, V. V., et al. 2000, A&A, 355, L27
Horner, J., Kane, S. R., Marshall, J. P., et al. 2020, PASP, 132, 102001
Hoyer, S., Guterman, P., Demangeon, O., et al. 2020, A&A, 635, A24
Hughes, A. M., Duchêne, G., & Matthews, B. C. 2018, ARA&A, 56, 541
Hunter, J. D. 2007, CSE, 9, 90
Ikoma, M., & Kobayashi, H. 2025, ARA&A, 63, 217
Ishihara, D., Onaka, T., Kataza, H., et al. 2010, A&A, 514, A1
Jang-Condell, H., Chen, C. H., Mittal, T., et al. 2015, ApJ, 808, 167
Jenkins, J. M., Twicken, J. D., McCauliff, S., et al. 2016, SPIE, 9913, 99133E
Karalis, A., Lee, E. J., & Thorngren, D. P. 2025, ApJ, 978, 46
Kaufer, A., Stahl, O., Tubbesing, S., et al. 1999, Msngr, 95, 8
Kipping, D. M. 2013, MNRAS, 434, L51

Kong, Z., Johansen, A., Lambrechts, M., Jiang, J. H., & Zhu, Z.-H. 2024, A&A, 687, A121
Koposov, S., Speagle, J., Barbary, K., et al. 2023, joshspeagle/dynesty: v2.1.1, Zenodo, doi:10.5281/zenodo.7832419
Kopparapu, R. K., Ramirez, R. M., SchottelKotte, J., et al. 2014, ApJL, 787, L29
Kraft, R. P. 1967, ApJ, 150, 551
Kral, Q., Matrà, L., Kennedy, G. M., Marino, S., & Wyatt, M. C. 2020, MNRAS, 497, 2811
Krivov, A. V., & Booth, M. 2018, MNRAS, 479, 3300
Lagrange, A.-M., Desort, M., Galland, F., Udry, S., & Mayor, M. 2009, A&A, 495, 335
Lebouteiller, V., Barry, D. J., Spoon, H. W. W., et al. 2011, ApJS, 196, 8
Lieman-Sifry, J., Hughes, A. M., Carpenter, J. M., et al. 2016, ApJ, 828, 25
Mandel, K., & Agol, E. 2002, ApJL, 580, L171
Marino, S., Matrà, L., Hughes, A. M., et al. 2026, A&A, 705, A195
Marshall, J. P., Milli, J., Choquet, E., et al. 2023, MNRAS, 521, 5940
Marshall, J. P., Muñoz-Gutiérrez, M. A., Sefilian, A. A., & Peimbert, A. 2026, MNRAS, 545, staf1990
Marton, G., Gezer, I., Madarász, M., et al. 2024, A&A, 688, A203
Matrà, L., Marino, S., Wilner, D. J., et al. 2025, A&A, 693, A151
Maxted, P. F. L., Ehrenreich, D., Wilson, T. G., et al. 2022, MNRAS, 514, 77
Mayor, M., Pepe, F., Queloz, D., et al. 2003, Msngr, 114, 20
McCormac, J., Pollacco, D., Skillen, I., et al. 2013, PASP, 125, 548
McCully, C., Volgenau, N. H., Harbeck, D.-R., et al. 2018, SPIE, 10707, 107070K
Mittal, T., Chen, C. H., Jang-Condell, H., et al. 2015, ApJ, 798, 87
Muñoz-Gutiérrez, M. A., Marshall, J. P., & Peimbert, A. 2023, MNRAS, 520, 3218
Mustill, A. J., & Wyatt, M. C. 2009, MNRAS, 399, 1403
NASA Exoplanet Archive 2019, Planetary Systems Composite Table, IPAC, doi:10.26133/NEA13
Parviainen, H. 2015, MNRAS, 450, 3233
Parviainen, H., & Aigrain, S. 2015, MNRAS, 453, 3821
Paunzen, E. 2015, A&A, 580, A23
Pearce, T. D., Krivov, A. V., Sefilian, A. A., et al. 2024, MNRAS, 527, 3876
Pepe, F., Mayor, M., Delabre, B., et al. 2000, SPIE, 4008, 582
Petit, A. C., Pichierri, G., Goldberg, M., & Morbidelli, A. 2025, in Dynamical Evolution of Planetary Systems, ed. H. J. Deeg & J. A. Belmonte (Springer)
Rando, N., Asquier, J., Corral Van Damme, C., et al. 2020, SPIE, 11443, 1144314
Rasmussen, C. E., & Williams, C. K. I. 2006, Gaussian Processes for Machine Learning (MIT Press)
Rein, H., & Liu, S. F. 2012, A&A, 537, A128
Rein, H., & Spiegel, D. S. 2015, MNRAS, 446, 1424
Ricker, G. R., Winn, J. N., Vanderspek, R., et al. 2014, SPIE, 9143, 914320
Riello, M., De Angeli, F., Evans, D. W., et al. 2021, A&A, 649, A3
Sandhaus, P., Dawson, R. I., MacDonald, M., Shakespeare, C. J., & Morrison, S. 2025, ApJ, 990, 61
Schmider, F.-X., Abe, L., Agabi, A., et al. 2022, SPIE, 12182, 121822O
Sefilian, A. A., Kratter, K. M., Wyatt, M. C., et al. 2025, MNRAS, 543, 3123
Skilling, J. 2004, AIPC, 735, 395
Skilling, J. 2006, BayAn, 1, 833
Skrutskie, M. F., Cutri, R. M., Stiening, R., et al. 2006, AJ, 131, 1163
Smith, J. C., Stumpe, M. C., Van Cleve, J. E., et al. 2012, PASP, 124, 1000
Speagle, J. S. 2020, MNRAS, 493, 3132
Spearman, C. 1904, Am. J. Psychol., 15, 72
Squicciarini, V., Mazoyer, J., Lagrange, A. M., et al. 2025, A&A, 693 A54
Stumpe, M. C., Smith, J. C., Catanzarite, J. H., et al. 2014, PASP, 126, 100
Stumpe, M. C., Smith, J. C., Van Cleve, J. E., et al. 2012, PASP, 124, 985
Suárez Mascareño, A., Damasso, M., Lodieu, N., et al. 2021, NatAs, 6, 232
Tang, J., Bressan, A., Rosenfield, P., et al. 2014, MNRAS, 445, 4287
Tang, Y., Fortney, J. J., Murray-Clay, R., & Broome, M. 2025, ApJ, 995, 20
Terrill, J., Marino, S., Booth, R. A., et al. 2023, MNRAS, 524, 1229
TESS Team 2021, TESS Light Curves—All Sectors, STScI/MAST, doi:10.17909/T9-NMC8-F686
Thébault, P. 2009, A&A, 505, 1269
Virtanen, P., Gommers, R., Oliphant, T. E., et al. 2020, NatMe, 17, 261
Wahhaj, Z., Milli, J., Kennedy, G., et al. 2016, A&A, 596, L4
Wheatley, P. J., West, R. G., Goad, M. R., et al. 2018, MNRAS, 475, 4476
Wittenmyer, R. A., Wang, S., Horner, J., et al. 2020, MNRAS, 492, 377
Wright, E. L., Eisenhardt, P. R. M., Mainzer, A. K., et al. 2010, AJ, 140, 1868
Wyatt, M. C., Dermott, S. F., Telesco, C. M., et al. 1999, ApJ, 527, 918
Yoshikawa, M. 1989, A&A, 213, 436
Youdin, A. N., & Zhu, Z. 2025, arXiv:2501.13214
Zakhozhay, O. V., Launhardt, R., Trifonov, T., et al. 2022, A&A, 667, L14
Zeng, L., Jacobsen, S. B., Sasselov, D. D., et al. 2019, PNAS, 116, 9723